

Probing fundamental physics with H_2^+

Master thesis

presented by

Angel Octavio Parada Flores

Internship carried out at
Laboratoire Kastler-Brossel/Université Évry Paris Saclay
under the supervision of
Laurent Hilico

Master degree of Physics
Erasmus Mundus QUARMEN

Paris, France - August 2025



Contents

| | | |
|----------|--|-----------|
| 1 | Introduction | 1 |
| I | Context and Motivation | 1 |
| I.1 | The Trapped Ions Team at Laboratoire Kastler Brossel | 1 |
| I.2 | Precision Tests of Fundamental Physics | 1 |
| II | Overview of the Experiment | 2 |
| II.1 | Femtosecond Lasers and Optical Frequency Combs | 4 |
| II.2 | Frequency Conversion Chain | 5 |
| II.3 | Experimental Setup Overview | 6 |
| III | Objective | 10 |
| 2 | Theory | 11 |
| I | Schrödinger Functions of H_2^+ | 11 |
| I.1 | Radial Wave Functions | 11 |
| I.2 | Magnetic and Hyperfine Interactions | 14 |
| I.3 | Zeeman Splitting | 17 |
| II | Two-Photon Spectroscopy | 19 |
| II.1 | Two Photon Operator | 19 |
| II.2 | Transition Matrix Elements | 21 |
| 3 | Methods and Results | 25 |
| I | Transition Energies | 25 |
| II | Spinless Matrix Elements | 28 |
| III | Two-Photon Probabilities per Unit Time | 31 |
| III.1 | General trends | 31 |
| III.2 | Behavior for $\bar{J} = 3/2$ | 33 |
| III.3 | Behavior for $\bar{J} = 5/2$ | 33 |
| III.4 | Magnetic Field dependence | 34 |
| IV | Light Shifts in Two-Photon Hyperfine Transitions | 35 |
| IV.1 | General Trends | 35 |
| IV.2 | Behavior for $\bar{J} = 3/2$ | 37 |
| IV.3 | Behavior for $\bar{J} = 5/2$ | 37 |
| IV.4 | Magnetic Field Dependence | 38 |
| V | Raman Rabi Frequencies | 39 |
| V.1 | General Trends | 39 |
| V.2 | Behavior for $\bar{J} = 3/2$ | 41 |
| V.3 | Behavior for $\bar{J} = 5/2$ | 41 |
| V.4 | Magnetic Field Dependence | 41 |
| VI | Light Shifts in Raman Transitions | 42 |
| VI.1 | General Trends | 42 |
| VI.2 | Behavior for $\bar{J} = 3/2$ | 44 |

| | | |
|----------|--|-----------|
| VI.3 | Behavior for $\bar{J} = 5/2$ | 44 |
| VI.4 | Magnetic Field Dependence | 44 |
| 4 | Conclusion | 45 |
| A | Wave Functions Variational Calculation | 49 |
| B | Linear Paul Trap | 50 |
| I | Linear Paul Trap | 50 |
| I.1 | Adiabatic Approximation and Micromotion | 51 |
| I.2 | Endcap Potential and Axial Confinement | 51 |
| C | Supplementary Results: Complete Data Sets for Two-Photon and Raman Calculations | 52 |

List of Figures

| | | |
|-----|---|----|
| 1.1 | Historical improvement in the measurement accuracy of the proton-to-electron mass ratio (m_p/m_e) over time, as reflected in CODATA [1] adjustments and various experimental results. The left panel shows the overall trend from 1970 to 2025, with a significant decrease in inaccuracy. The zoomed-in right panel highlights recent advancements (2012-2025), differentiating between results from Penning trap measurements and HD ⁺ spectroscopy. | 2 |
| 1.2 | Scheme of the SI-referenced lasers in the H ₂ ⁺ experiment at LKB and its purpose. | 2 |
| 1.3 | (a) Time-domain pulse train showing carrier-envelope phase slips; (b) Corresponding frequency-domain comb structure with evenly spaced modes separated by f_{rep} , offset by the carrier-envelope offset f_0 [2]. | 4 |
| 1.4 | CO ₂ laser frequency comb scheme [3]. | 7 |
| 1.5 | Optical lock to REFIMEVE ultrastable signal scheme [3] | 7 |
| 1.6 | Linear Paul trap with its eight electrodes and the corresponding electric connections. [4] | 8 |
| 1.7 | Fluorescence images of typical Be ⁺ - H ₂ ⁺ ion crystals produced in the Trapped Ion group at LKB. The blue color indicates fluorescence from laser-cooled Be ⁺ ions, while the encircled dark spots on the left image and the dark stripe at the center of the right image indicate non-fluorescing H ₂ ⁺ ions. | 8 |
| 1.8 | The arrows show the vibrational ground state preparation of H ₂ ⁺ using a 3+1 REMPI scheme at 303 nm ①, and after that the 2+1 REMPD spectroscopy ②+③. The inset shows the two-photon transition at 9.17 μm between two ro-vibrational levels [4, 3]. | 9 |
| 2.1 | Order-of-magnitude diagram of the energy scales relevant in this work. The hyperfine structure lies far below the rovibrational splittings and requires high-precision modeling to resolve. | 15 |
| 2.2 | Energy levels of the hyperfine states for both rovibrational levels as a function of the applied magnetic field B in the range 0–200 Gauss. | 18 |
| 2.3 | Energy levels of the hyperfine states for both rovibrational levels as a function of the applied magnetic field B in the range 0–2 Gauss. | 18 |
| 2.4 | Two-photon rovibrational transition at resonance. | 22 |
| 2.5 | Raman transition occurring within the same rovibrational state and involving different hyperfine sublevels. | 23 |
| 2.6 | ac Stark shifts experienced by a hyperfine level under two-photon illumination. . | 24 |

| | | |
|-----|---|----|
| 3.1 | Calculated two-photon transition energies as a function of magnetic field (0–15 G) for $ \bar{J}, M_J\rangle \rightarrow \bar{J}, M'_J\rangle$ transitions, shown for polarization components $q = 0$ (left) and $q = 1$ (right). For $q = 1$, the transitions exhibit a dominant linear Zeeman splitting, while for $q = 0$, nonlinear behavior persists, especially in states with strong hyperfine mixing. The region highlighted by a square corresponds to the low-field regime explored in detail in Figure 3.2. Note: The y -axis units differ among the panels and must be read carefully. | 26 |
| 3.2 | Zoomed-in view of the low-field regime (0–0.1 G) corresponding to the boxed region in Figure 3.1. In this regime, the hyperfine interaction dominates. For $q = 1$, the Zeeman shifts are small but linear, while for $q = 0$, the transition energies exhibit predominantly nonlinear (quadratic) dependence on B , characteristic of mixed states. Note: The y -axis units differ among the panels and must be read carefully. | 27 |
| 3.3 | Reduced Matrix Elements $\langle \nu L Q^{(k)} \nu' L' \rangle \equiv \langle \nu L Q^{(k)} \nu' L' \rangle / (\sqrt{2L+1})$ for the Raman Rabi frequency calculations for the states $ \nu = 0, L = 2\rangle$ (top) and $ \nu = 0, L = 2\rangle$ (bottom) across different wavelengths. The red-dotted line represents the static polarizability ($\lambda \rightarrow \infty$) found in [5]. | 29 |
| 3.4 | Two Photon Rovibrational Transitions for two polarization configurations. Each subpanel shows the corresponding magnetic field strength and transition type. Local labels are not comparable across panels. | 32 |
| 3.5 | Two Photon Rovibrational Transitions for (σ^+, σ^+) polarization configuration. Each subpanel shows the corresponding magnetic field strength and transition type. Local labels are not comparable across panels. | 33 |
| 3.6 | Two-photon light shifts for two polarization configurations. Each subpanel shows the corresponding magnetic field strength and transition type. Local labels are not comparable across panels. | 36 |
| 3.7 | Raman Rabi Frequencies for two polarization configurations. Each subpanel shows the corresponding magnetic field strength and transition type. Local labels are not comparable across panels. | 40 |
| 3.8 | Raman light shifts for two polarization configurations. Each subpanel shows the corresponding magnetic field strength and transition type. Local labels are not comparable across panels. | 43 |
| B.1 | Stability diagram of the Mathieu equation for a linear RF trap [4]. Left: overlapping regions define stable solutions. Right: the first stable region. | 51 |
| C.1 | Comprehensive results for two-photon transition probabilities for all polarization configurations (q_1, q_2) and magnetic fields $B = 0$ and 1 G. Local labels within each panel are not directly comparable across different subfigures. | 52 |
| C.2 | Comprehensive results for two-photon transition probabilities for all polarization configurations (q_1, q_2) and magnetic fields $B = 0$ and 1 G. Local labels within each panel are not directly comparable across different subfigures. | 53 |
| C.3 | Comprehensive results for two-photon light shifts for all polarization configurations (q_1, q_2) and magnetic fields $B = 0$ and 1 G. Local labels within each panel are not directly comparable across different subfigures. | 54 |
| C.4 | Comprehensive results for Raman Rabi Frequencies for all polarization configurations (q_1, q_2) and magnetic fields $B = 0$ and 1 G. Local labels within each panel are not directly comparable across different subfigures. | 55 |
| C.5 | Comprehensive results for Raman light shifts for all polarization configurations (q_1, q_2) and magnetic fields $B = 0$ and 1 G. Local labels within each panel are not directly comparable across different subfigures. | 55 |

List of Tables

| | | |
|-----|--|----|
| 2.1 | Hyperfine splittings (in MHz) and reduced matrix elements of L_e and L_1 (divided by $\sqrt{2L+1}$) for the rovibrational levels (ν, L) with $L = 2$ and $\nu = 0, 1$ of H_2^+ . The values of $\langle\langle L_{\text{tot}} \rangle\rangle$ are not explicitly listed, but the last column shows the corresponding rotational g factors. Data from [6, 7]. | 17 |
| 2.2 | Values of the coefficient $a_q^{(k)}$ for all combinations of the standard polarizations. | 21 |

Abstract

This internship report outlines work performed within the Trapped Ions team at Laboratoire Kastler Brossel (LKB), a leading research institution focusing on high-precision measurements to test fundamental physical theories. The team's primary experimental goal is to precisely determine the proton-to-electron mass ratio (μ) through the measurement of a specific two-photon transition in the H_2^+ ion, aiming for an unprecedented experimental uncertainty of 1×10^{-12} . The present work of this internship was focused on exploring the fundamental properties of H_2^+ through numerical simulations for future measurements in this molecule.

This internship was conducted under the supervision of Laurent Hilico, with the valuable assistance of doctoral researcher Maxime Leuliet and the support of researcher Jean-Philippe Karr.

Chapter 1

Introduction

I Context and Motivation

I.1 The Trapped Ions Team at Laboratoire Kastler Brossel

The Laboratoire Kastler Brossel (LKB) is a joint research unit affiliated with the École Normale Supérieure, Sorbonne University, the Collège de France, and the National Centre for Scientific Research (CNRS). Within LKB, the Trapped Ions team leverages the unique properties of cold, trapped ions to conduct high-precision measurements. Their research aims to rigorously test physical theories and enhance our understanding of fundamental physical constants. This team uniquely combines both theoretical and experimental approaches to study the H_2^+ ion.

I.2 Precision Tests of Fundamental Physics

Numerous high-precision experiments are currently underway to test the Standard Model of physics. These efforts have two primary objectives: first, to refine the values of fundamental constants, as maintained by CODATA [8]; and second, to search for physics beyond the Standard Model.

Among the simplest and most precisely calculable molecular systems are the hydrogen molecular ions H_2^+ and HD^+ . Each of these ions consists of only two nuclei and a single electron. The transition frequencies within these systems are directly sensitive to the proton-to-electron mass ratio, $\mu = m_p/m_e$, since Hydrogen molecular ions are calculable quantum systems. This sensitivity allows for extremely precise determinations of this crucial fundamental constant. Recent measurements on HD^+ have already improved the accuracy of μ to 2×10^{-11} [9], with further improvements expected using H_2^+ [10, 11, 12].

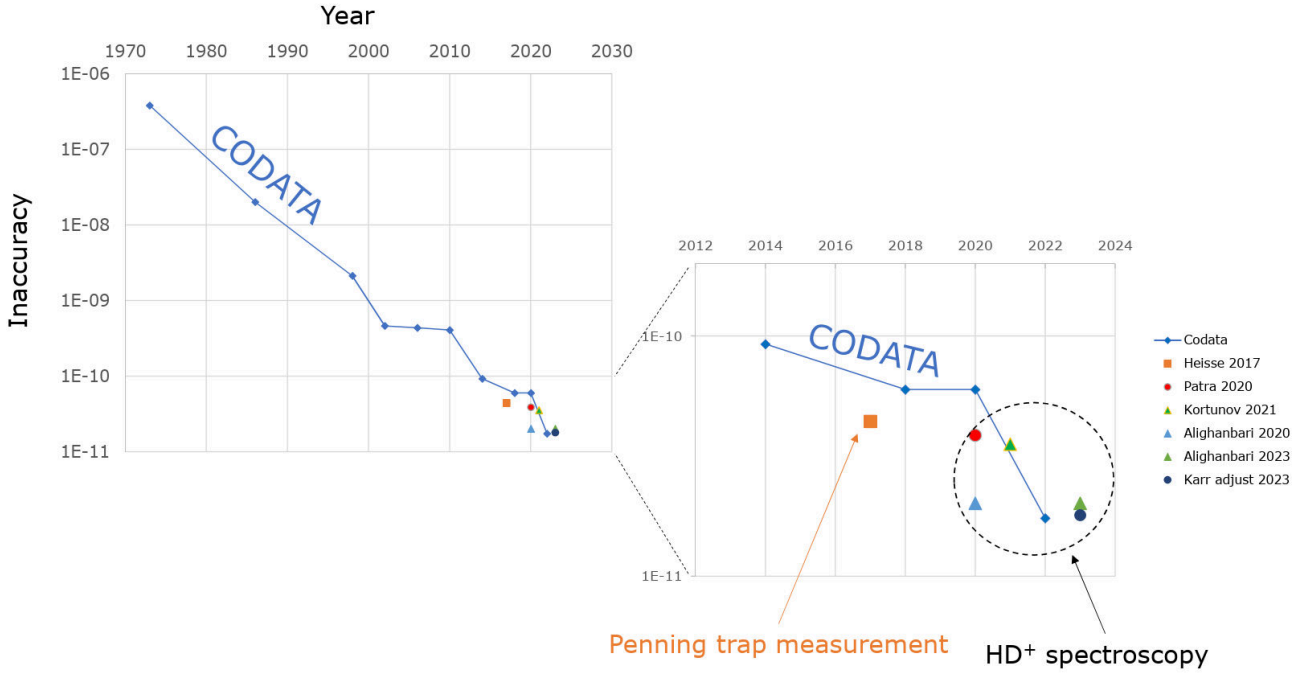


Figure 1.1: Historical improvement in the measurement accuracy of the proton-to-electron mass ratio (m_p/m_e) over time, as reflected in CODATA [1] adjustments and various experimental results. The left panel shows the overall trend from 1970 to 2025, with a significant decrease in inaccuracy. The zoomed-in right panel highlights recent advancements (2012-2025), differentiating between results from Penning trap measurements and HD^+ spectroscopy.

II Overview of the Experiment

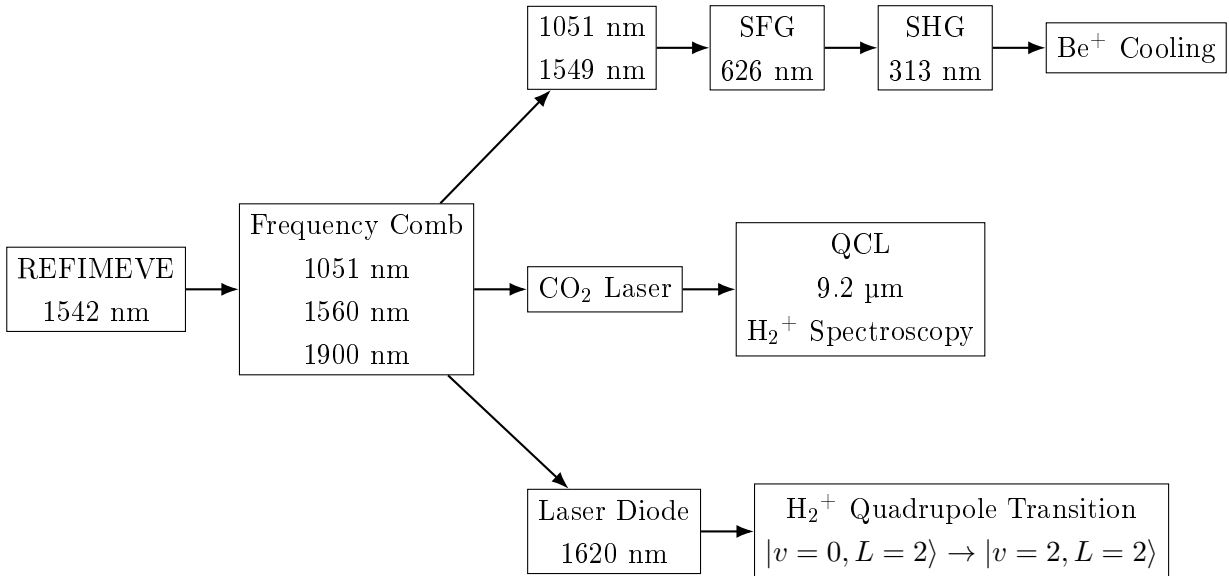


Figure 1.2: Scheme of the SI-referenced lasers in the H_2^+ experiment at LKB and its purpose.

The experiment conducted at LKB aims to measure with high precision the two-photon transition frequency between the ro-vibrational levels $1s\sigma_g |\nu = 0, L = 2\rangle \rightarrow |\nu = 1, L = 2\rangle$ of the H_2^+ molecular ion. To suppress first-order Doppler shifts, a major limitation in precision spectroscopy, the transition is driven using two counter-propagating photons, which effectively cancel the Doppler effect in the laboratory frame.

The H_2^+ ions are prepared in a well-defined quantum state using Resonance Enhanced Multi-Photon Ionization (REMPI), a 3+1 photon ionization process at 303 nm. This method selectively ionizes neutral H_2 molecules into the desired $|\nu = 0, L = 2\rangle$ ro-vibrational level of the ion. The resulting H_2^+ ions are then trapped in a linear radiofrequency trap that ensures confinement and isolation from environmental perturbations.

Due to the homonuclear and symmetric nature of H_2^+ , one-photon electric dipole transitions are strongly suppressed, making two-photon transitions the dominant excitation mechanism. Despite their low transition probabilities, the high spectral resolution enabled by Doppler-free two-photon spectroscopy makes this approach ideal for probing such forbidden transitions with exceptional accuracy.

At the target precision level of 10^{-12} , the second-order Doppler shift becomes a significant consideration. This relativistic effect is given by:

$$\frac{\Delta\nu}{\nu} = \frac{v^2}{2c^2} = \frac{\frac{1}{2}mv^2}{mc^2}.$$

For H_2^+ ions with a typical kinetic energy of approximately 1 eV and a rest mass energy of about 2 GeV, this corresponds to a relative shift of roughly 5×10^{-10} . To mitigate this uncertainty, the ions must be cooled to very low temperatures. Unfortunately, laser cooling is not feasible for H_2^+ due to its forbidden dipole transitions. Instead, sympathetic cooling is employed: another ionic species, specifically Be^+ , is laser-cooled in the same trap, and H_2^+ is subsequently cooled via Coulomb interaction with the cold Be^+ ions. Beryllium ions are ideal for this purpose due to their light mass and a convenient cooling transition at 313 nm.

The spectroscopy laser used for this experiment is a 9.17 μm quantum cascade laser (QCL), precisely locked to a CO_2 laser. Given the weak nature of the two-photon transition, a Fabry-Perot cavity placed in vacuum is used to enhance the beam intensity and maximize the interaction strength with the trapped ions. To ensure optimal alignment between the ions and the fixed-mode spectroscopy beam, the ion trap is mounted on a translation stage, and its position has been optimized.

Detection of the excited ions is carried out via Resonance Enhanced Multi-Photon Dissociation (REMPD). After excitation to the $|\nu = 1, L = 2\rangle$ state, a 213 nm laser is used to dissociate the molecule. The dissociation cross-section at 213 nm is 72 times higher for the $\nu = 1$ state than for the $\nu = 0$ state. This significant difference enables highly state-selective detection by monitoring the loss of ions from the trap. The loss rate is much higher if the H_2^+ ions are promoted to the $\nu = 1$ level by the spectroscopy laser.

Utilizing a narrow-linewidth 9.17 μm laser (~ 100 Hz), we aim for an unprecedented experimental uncertainty of 1×10^{-12} . Current theoretical predictions for this transition achieve an accuracy of 7.6×10^{-12} [13].

This high-precision measurement of the $|\nu = 0, L = 2\rangle \rightarrow |\nu = 1, L = 2\rangle$ transition in H_2^+ will provide a direct optical determination of the proton-to-electron mass ratio, μ , thereby contributing significantly to tests of fundamental physics at the highest level of precision.

II.1 Femtosecond Lasers and Optical Frequency Combs

Femtosecond lasers emit pulses of light with durations on the order of 10^{-15} seconds. These ultrashort pulses are generated via mode-locking, a technique that forces multiple longitudinal modes of the laser cavity to oscillate with fixed phase relationships.

Mode-locking can be achieved either actively, by modulating cavity losses at the round-trip frequency using an external signal (e.g., RF-driven electro-optic modulators), or passively, by incorporating a saturable absorber that favors high-intensity pulse formation. Passive mode-locking is especially effective with broadband gain media, enabling the simultaneous excitation of many cavity modes. The coherent superposition of these modes leads to the formation of a stable train of ultrashort pulses, with pulse duration τ_p and repetition period

$$T_{\text{rep}} = \frac{L}{v_g},$$

where L is the cavity length and v_g is the group velocity of the pulse envelope.

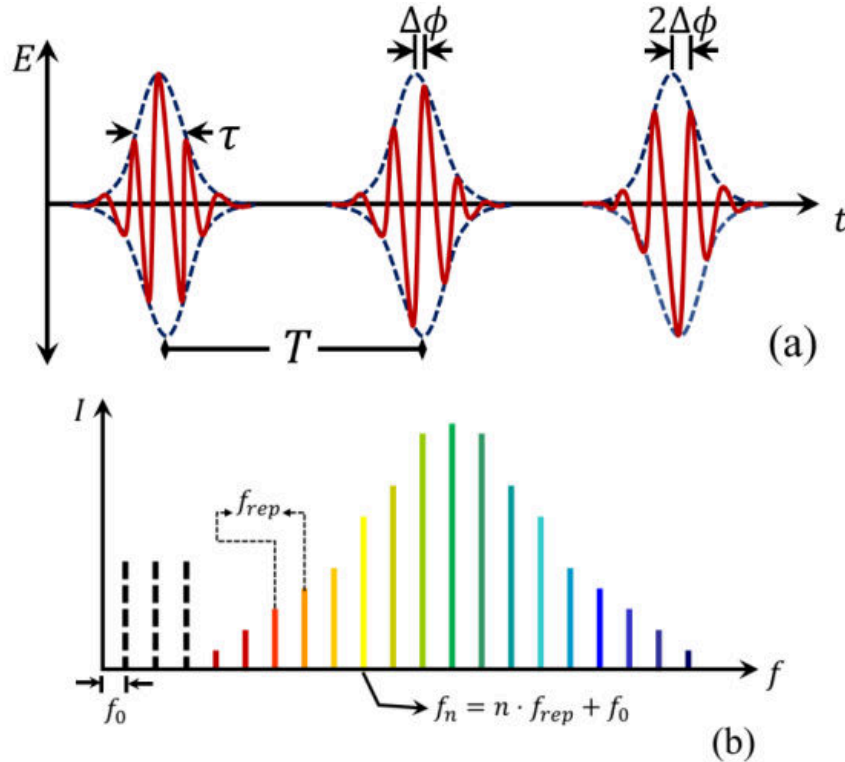


Figure 1.3: (a) Time-domain pulse train showing carrier-envelope phase slips; (b) Corresponding frequency-domain comb structure with evenly spaced modes separated by f_{rep} , offset by the carrier-envelope offset f_0 [2].

In the frequency domain, this mode-locked pulse train corresponds to a comb of narrow

spectral lines with frequencies given by:

$$\nu_n = n f_{\text{rep}} + f_0,$$

where f_{rep} is the repetition rate of the pulses, n is an integer mode index, and f_0 is the carrier-envelope offset (CEO), arising from dispersion-induced phase slips between the pulse envelope and carrier wave. The CEO is related to the per-round-trip phase slip $\Delta\phi$ by:

$$f_0 = \frac{\Delta\phi}{2\pi T_{\text{rep}}}.$$

The resulting structure, an Optical Frequency Comb (OFC), is an evenly spaced set of optical frequencies spanning hundreds of terahertz. When both f_{rep} and f_0 are stabilized, this comb acts as a precise optical ruler that can connect optical and microwave frequencies with high accuracy

II.1.1 Beat Note Detection and Laser Locking

To stabilize laser frequencies in the experiment, fiber lasers at 1550 nm and 1051 nm are phase-locked to specific modes of the optical frequency comb. Beat notes are generated by mixing each laser with the nearest comb mode on a fast photodetector. The resulting radio-frequency signal — the beat frequency — corresponds to the difference between the laser and the comb mode.

The beat note is first amplified using a ZFL amplifier and then passed through a frequency divider with division factor 8, which reduces it to a lower intermediate frequency suitable for digital processing. This signal is compared to a reference frequency f_{ref} using a Phase-Frequency Comparator (PFC), which generates an error signal. This error signal is processed by a Proportional-Integral (PI) controller that adjusts the laser's injection current or cavity length, keeping it locked to the comb.

Each laser is stabilized in a similar manner, with a tunable offset introduced to control the frequency separation between the two lasers. The same architecture is applied to the 1051 nm system, allowing for precise referencing to the optical comb.

II.2 Frequency Conversion Chain

Once stabilized, the 1051 nm laser undergoes a series of nonlinear optical processes to generate coherent ultraviolet light at 313 nm. After spectral filtering to eliminate amplified spontaneous emission, the beam is amplified to the power levels required for nonlinear conversion.

The first nonlinear stage is sum-frequency generation (SFG), where the 1051 nm beam and a second 1550 nm beam are mixed in a nonlinear crystal to produce 626 nm light:

$$\frac{1}{\lambda_{626}} = \frac{1}{\lambda_{1051}} + \frac{1}{\lambda_{1550}}.$$

The 626 nm output is then frequency-doubled via second-harmonic generation (SHG), yielding ultraviolet light at 313 nm:

$$\frac{1}{\lambda_{313}} = 2 \cdot \frac{1}{\lambda_{626}}.$$

This narrowband UV light is used for spectroscopy and manipulation of beryllium ions (Be^+), as it is resonant with their transitions. Because the original lasers are locked to the frequency comb, the UV output inherits the comb's frequency stability and traceability.

II.3 Experimental Setup Overview

The experiment involves high-resolution spectroscopy of state-selected H_2^+ ions confined in a linear RF Paul trap and sympathetically cooled via co-trapped Be^+ ions. The setup comprises five main components: the frequency comb, a laser frequency stabilization system, the ion trap, the state preparation system, and the laser system for spectroscopy and detection.

- **Optical Frequency Comb:** The frequency comb is a 1550 nm f_{ceo} -free comb, optically locked to a 1542 nm reference signal disseminated by the REFIMEVE fiber network [14]. The comb extends spectrally to 1900 nm and provides SI-traceable frequencies of the form $f_q = qf_{\text{rep}}$ with $f_{\text{rep}} = 200$ MHz.
- **CO₂ Laser Stabilization via Sum-Frequency Generation**

The frequency of a 9.17 μm CO₂ laser is stabilized using SFG with a 1.895 μm comb mode in an AgGaSe₂ crystal, producing 1.560 μm output. The powers involved are 18 mW (1.895 μm), 80 mW (CO₂), and the resulting SFG power is ~ 600 nW, with an efficiency of 0.7 mW/W² [15].

The beat note with the comb provides an error signal:

$$f_{\text{beat}} = f_{\text{CO}_2} - (q_2 - q_1)f_{\text{rep}},$$

where q_1 and q_2 are integer mode numbers representing specific spectral lines (or modes) of the optical frequency comb. The term $(q_2 - q_1)f_{\text{rep}}$ thus represents the frequency difference between two chosen comb modes. Here, $(q_2 - q_1) = 163\,541$. This signal is divided by 8, compared with a reference frequency via a Phase-Frequency Comparator (PFC), and used to correct the CO₂ laser frequency through a Proportional-Integral (PI) controller.

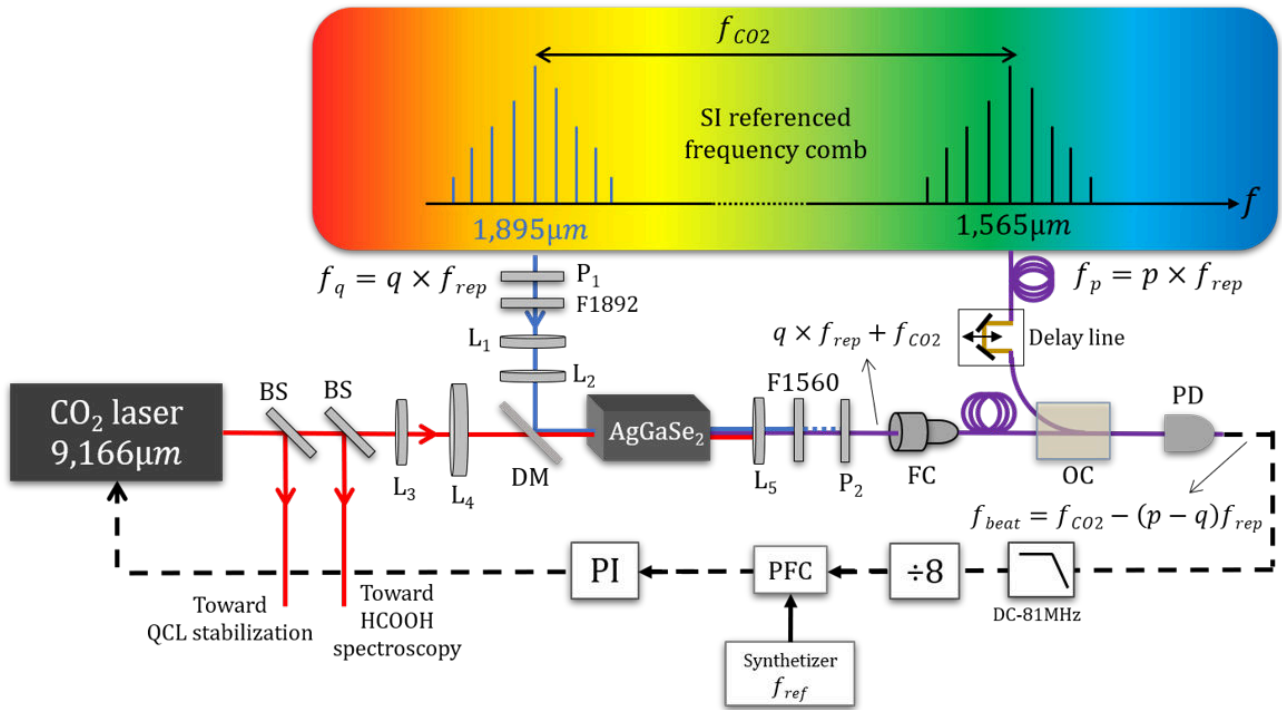


Figure 1.4: CO₂ laser frequency comb scheme [3].

• Laser Frequency Stabilization

The laser system is referenced to the SI second using a stabilized frequency comb (Toptica DFC 200 at 1.565 μm) and the REFIMEVE ultra stable 1.542 μm source [14]. These signals are combined via Dense Wavelength Division Multiplexing (DWDM), a 25% coupler (CP), and an Optical Circulator (OC). A photodiode detects the beat note at 89.5 MHz, which is filtered, monitored, and analyzed using a spectrum analyzer. The frequency instability of the optical lock is below 2×10^{-13} at 1 s.

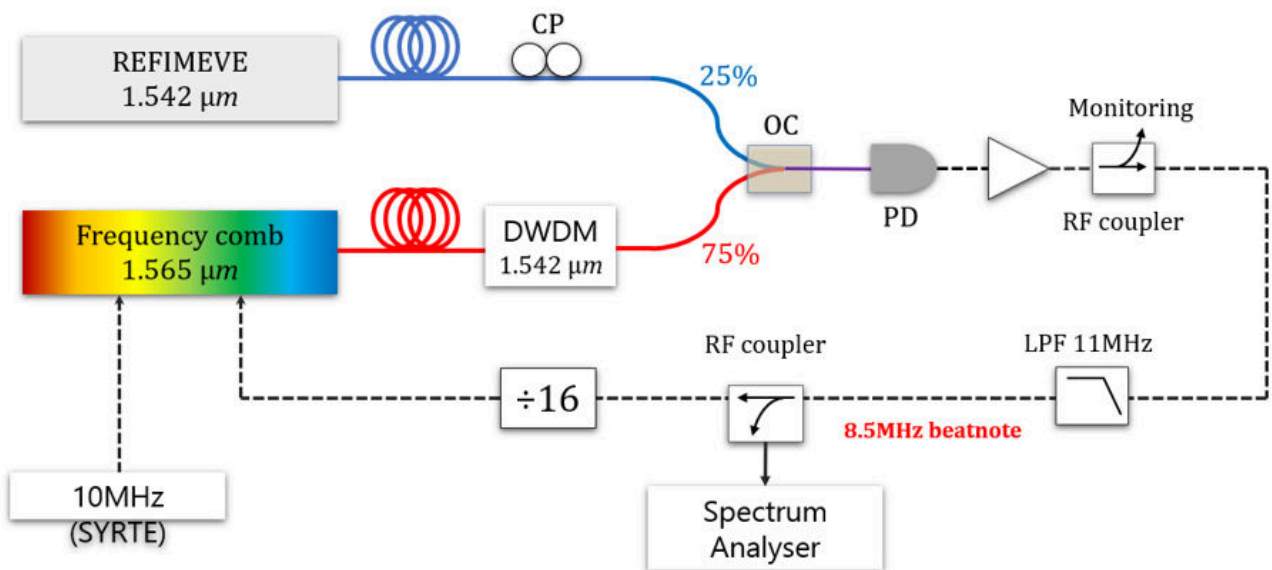


Figure 1.5: Optical lock to REFIMEVE ultrastable signal scheme [3]

- Ion Trap and Cooling:** The RF Paul trap has a characteristic radius $R_0 = 3.5$ mm and operates at a drive frequency of 13 MHz with an RF voltage up to 500 V, resulting in a trap depth of approximately 1 eV. A 313 nm laser is used to Doppler-cool the Be^+ ions. The H_2^+ ions are cooled sympathetically through Coulomb interaction, forming a mixed-species crystal approximately 1.2 mm long along the z -axis. A theoretical overview of the Paul trap operation is provided in Appendix B

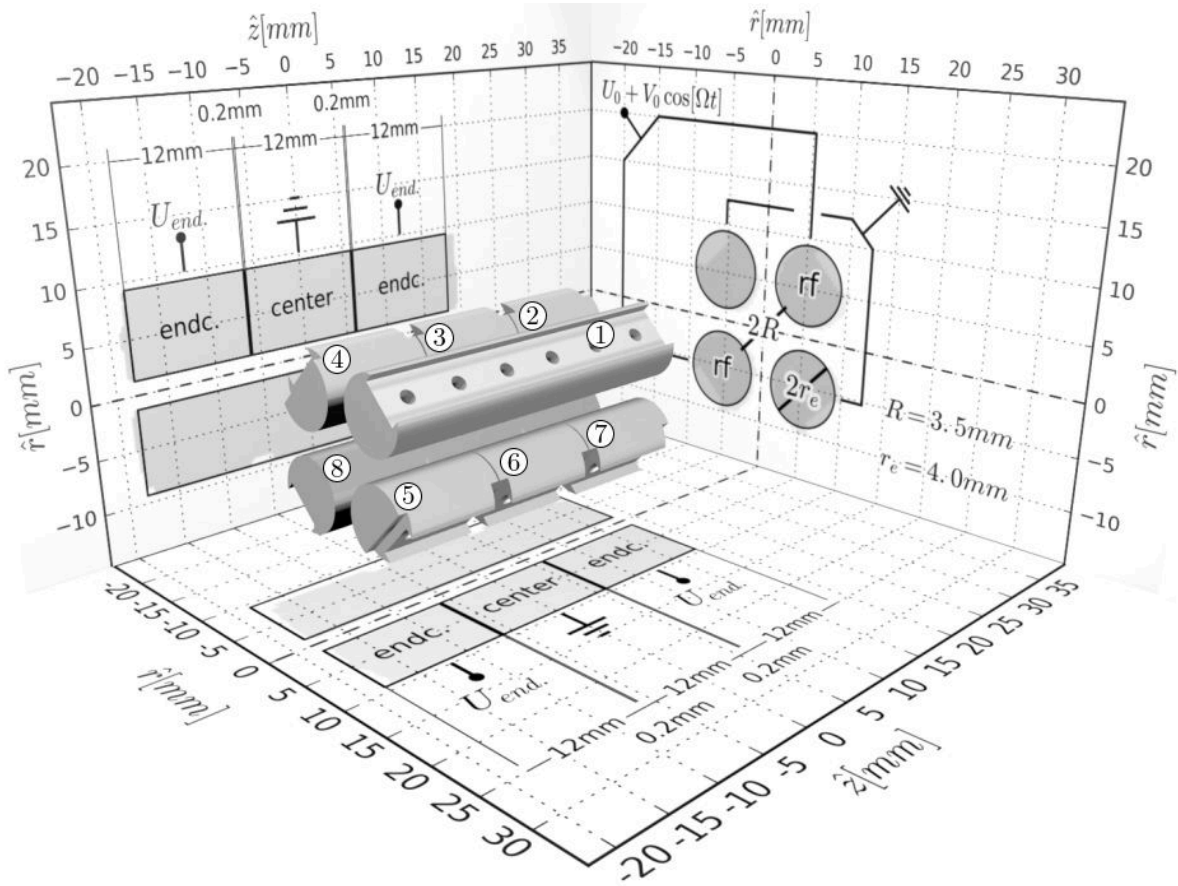


Figure 1.6: Linear Paul trap with its eight electrodes and the corresponding electric connections. [4]

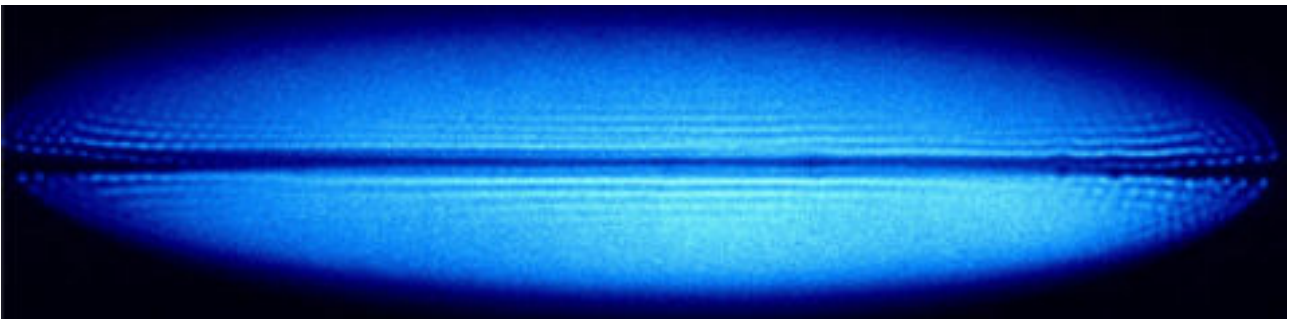


Figure 1.7: Fluorescence images of typical $\text{Be}^+ - \text{H}_2^+$ ion crystals produced in the Trapped Ion group at LKB. The blue color indicates fluorescence from laser-cooled Be^+ ions, while the encircled dark spots on the left image and the dark stripe at the center of the right image indicate non-fluorescing H_2^+ ions.

- State Preparation via REMPI

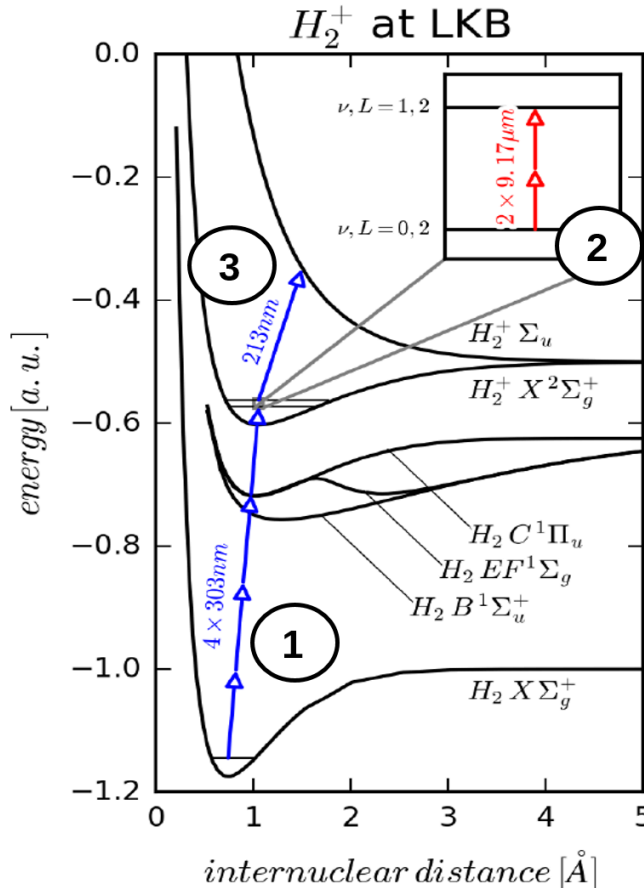


Figure 1.8: The arrows show the vibrational ground state preparation of H_2^+ using a 3+1 REMPI scheme at 303 nm (①), and after that the 2+1 REMPD spectroscopy (②)+(③). The inset shows the two-photon transition at 9.17 μm between two ro-vibrational levels [4, 3].

Although radiative decay in H_2^+ is highly suppressed due to its homonuclear structure, direct ionization methods such as electron impact would typically populate a broad distribution of rovibrational states. To ensure state-selective preparation, we instead employ a 3+1 Resonance-Enhanced Multi-Photon Ionization (REMPI) scheme at 303 nm (see Figure 1.8).

Neutral H_2 molecules in the ground state $X^1\Sigma_g^+(v=0, L=2)$ absorb three photons at 303 nm, reaching resonantly the excited state $C^1\Pi_u(v=0, L')$, followed by a fourth photon that ionizes the molecule (Fig. 1.8 step ①), yielding $H_2^+(v=0, L=2)$ with an estimated selectivity of 90%.

- Laser Parameters and Spectroscopy

The 303 nm radiation used for REMPI is generated via second-harmonic generation from a pulsed dye laser. The laser operates at 20 Hz, with a pulse energy of 3–4 mJ, a pulse duration of 10 ns, and a beam waist of $w_0 \approx 10 \mu\text{m}$, resulting in peak intensities of approximately $2.5 \text{ GW}/\text{mm}^2$.

The narrow two-photon transition at 9.17 μm (step ② in Fig. 1.8) is probed using Doppler-free spectroscopy. The mid-infrared laser beam is coupled into a high-finesse

Fabry–Pérot cavity installed under vacuum around the ion trap, which cancels the first-order Doppler shift.

The optical cavity provides a power build-up factor of about 160, with an input power of 20 mW leading to an intracavity power of roughly 3.2 W. With a beam waist of $w_0 \approx 300 \mu\text{m}$ at the ion location, this corresponds to an effective intensity of $I \approx \frac{2P}{\pi w_0^2} \approx 2.3 \times 10^7 \text{ W/m}^2 \approx 23 \text{ W/mm}^2$, which is the optical power effectively interacting with the ions.

- **State-Selective Photodissociation**

State detection is performed via photodissociation using a 213 nm pulsed laser (fifth harmonic of a YVO₄ source) operating at 10 kHz with 170 mW output power. This UV light promotes the molecule to a dissociative electronic state (Fig. 1.8 step ③), allowing detection of specific rovibrational states.

III Objective

The objective of this internship was to support the experimental efforts of the Trapped Ions team at Laboratoire Kastler Brossel by developing a theoretical and numerical framework to simulate two-photon spectroscopy in the H₂⁺ ion. The work focused on computing transition amplitudes for rovibrational two-photon processes, evaluating Rabi frequencies for Raman-type intra-rovibrational transitions, and quantifying AC Stark shifts through dynamic polarizability calculations. These simulations provide key insights into light–matter interaction regimes relevant for high-precision measurements and help optimize experimental parameters for future determinations of the proton-to-electron mass ratio.

Chapter 2

Theory

I Schrödinger Functions of H_2^+

Understanding the wave functions of H_2^+ is essential for its precise spectroscopic study. The relevant notations for describing its states are:

- $S_e = 1/2$: the electron spin.
- $I_1 = 1/2$ and $I_2 = 1/2$: the spins of the two protons.
- $I = I_1 + I_2$: the total nuclear spin.
- L_e : the orbital angular momentum of the electron.
- L_1 and L_2 : the orbital angular momentum of the two protons.
- L : the total orbital angular momentum.

It is crucial to note that due to the Pauli symmetrization principle, and considering that the electron occupies the ground $1s\sigma_g$ state, the total nuclear spin I is related to the orbital angular momentum L . Specifically, $I = 0$ when L is even, and $I = 1$ when L is odd. This spin-symmetry constraint significantly influences the allowed transitions and spectroscopic properties of H_2^+ .

I.1 Radial Wave Functions

The hydrogen molecular ion, H_2^+ , is a three-body system governed primarily by Coulomb interactions. In the laboratory frame, such a system can be described by the non-relativistic Hamiltonian:

$$H = - \sum_{i=1}^3 \frac{1}{2m_i} \nabla_{\mathbf{R}_i}^2 + \sum_{1 \leq i < j \leq 3} \frac{q_i q_j}{|\mathbf{R}_i - \mathbf{R}_j|}, \quad (2.1)$$

where m_i , q_i , and \mathbf{R}_i denote the mass, charge, and position of the i -th particle, respectively.

We assume that particles 1 and 2 are identical nuclei (each with charge Ze and mass M), and particle 3 is the electron with mass m_e and charge $-e$.

To solve the Schrödinger equation for this system, Hylleraas [16] introduced three interparticle distances as independent variables: r_1 , r_2 , and r_{12} , which characterize the shape and size of the triangle formed by the three particles.

Since the total momentum $\mathbf{P} = \mathbf{p}_1 + \mathbf{p}_2 + \mathbf{p}_3$ is conserved, we can separate out the center-of-mass motion. Defining the center-of-mass coordinate as

$$\mathbf{X} = \frac{1}{\sum_i m_i} \sum_{i=1}^3 m_i \mathbf{R}_i,$$

and introducing internal coordinates $\mathbf{r}_i = \mathbf{R}_i - \mathbf{X}$, the kinetic energy in the center-of-mass frame becomes:

$$T = - \sum_{i=1}^3 \frac{1}{2\mu_i} \nabla_{\mathbf{r}_i}^2,$$

where μ_i are the appropriate reduced masses.

Switching to atomic units via the substitutions $r = a_0 \tilde{r}$, $p = \frac{\hbar}{a_0} \tilde{p}$, with the Bohr radius defined by

$$a_0 = \frac{4\pi\epsilon_0 \hbar^2}{m_e e^2},$$

the dimensionless Hamiltonian becomes:

$$\hat{H} = \frac{1}{2\mu} (\nabla_1^2 + \nabla_2^2) + \frac{1}{m_e} \nabla_1 \cdot \nabla_2 + \frac{1}{m_e} \left(\frac{1}{\tilde{r}_{12}} - \frac{1}{\tilde{r}_1} - \frac{1}{\tilde{r}_2} \right). \quad (2.2)$$

The total angular momentum operator is given by:

$$\mathbf{L} = -i\mathbf{r}_1 \times \nabla_{\mathbf{r}_1} - i\mathbf{r}_2 \times \nabla_{\mathbf{r}_2}.$$

To solve the eigenvalue problem associated with the Hamiltonian \hat{H} , a variational approach is employed by seeking simultaneous eigenstates of a set of commuting operators: $\{\hat{H}, \mathbf{L}^2, L_z, \hat{\Pi}\}$, where \mathbf{L}^2 and L_z are the total orbital angular momentum and its projection along the quantization axis, respectively, and $\hat{\Pi}$ is the parity operator. For systems with well-defined orbital angular momentum quantum number L , the eigenvalues of $\hat{\Pi}$ are given by $(-1)^L$, reflecting the symmetry of the wavefunction under spatial inversion.

Following the methodology presented in [17], the time-independent Schrödinger equation is reformulated into a linear system of coupled differential equations. These equations are then solved numerically to obtain the energy eigenvalues and corresponding eigenfunctions. In the chosen coordinate system, the total wavefunction $\Psi_{LM}^{\Pi}(\mathbf{R}, \mathbf{r}_1)$ can be expanded in a basis of coupled spherical harmonics and radial functions as

$$\Psi_{LM}^{\Pi}(\mathbf{R}, \mathbf{r}_1) = \sum_{l_1, l_2} \mathcal{Y}_{LM}^{l_1 l_2}(\hat{\mathbf{R}}, \hat{\mathbf{r}}_1) G_{l_1 l_2}^{L\Pi}(R, r_1, r_2), \quad (2.3)$$

where $\mathcal{Y}_{LM}^{l_1 l_2}(\hat{\mathbf{R}}, \hat{\mathbf{r}}_1)$ are the bipolar harmonics that account for the angular dependencies, and the functions $G_{l_1 l_2}^{L\Pi}(R, r_1, r_2)$ describe the radial and interparticle correlations in the system.

The radial functions are expanded as

$$G_{l_1 l_2}^{L\Pi}(R, r_1, r_2) = \sum_{n=1}^N [C_n \text{Re}(e^{-\alpha_n R - \beta_n r_1 - \gamma_n r_2}) + D_n \text{Im}(e^{-\alpha_n R - \beta_n r_1 - \gamma_n r_2})].$$

This choice of basis ensures the correct angular momentum and parity properties, allowing for an efficient and accurate variational treatment of the three-body problem.

By convention, the total energy of a quantum system is measured relative to the dissociation threshold, defined as the limit in which all particles are infinitely separated and at rest. In this limit, the potential energy vanishes and the kinetic energy is zero (see Equation (2.1)), corresponding to a total energy of zero. This choice of energy origin allows bound-state energies to be interpreted directly as negative quantities, with deeper negative values indicating stronger binding.

In atomic units (a.u.), the unit of energy (known as the Hartree) is defined by setting the fundamental constants $\hbar = m_e = e = 1$, which leads to the expression $E_h = m_e c^2 \alpha^2 = \frac{\hbar^2}{m_e a_0^2}$. The Rydberg unit of energy is defined as exactly half a Hartree $1 \text{ Ry} = \frac{1}{2} E_h \approx 13.60569312 \text{ eV}$ according to CODATA22 [18]. Therefore, any energy expressed in atomic units can be converted to electronvolts using the relation $E [\text{eV}] = E [\text{a.u.}] \times 2 \text{ Ry}$.

In practical few-body calculations, such as for the H_2^+ ion, the Hamiltonian is rescaled using dimensionless units based on a reduced mass normalization. The code handed for this task, developed by V.I.Korobov and discussed later in Appendix A, defines a scaling factor $S = \frac{\min(m_i)}{m_e}$, where $\min(m_i)$ is the smallest mass in the system (typically the electron mass m_e). This ensures that the smallest particle has unit mass and all other masses are rescaled accordingly. The corresponding energy scaling factor is then defined as $E_S = 2 \text{ Ry} \cdot S$. This factor allows for conversion of dimensionless eigenvalues ϵ obtained from the rescaled Hamiltonian into physical energy units.

Within the Born–Oppenheimer approximation, the asymptotic value of the potential energy curve for the $1s\sigma_g$ electronic ground state corresponds to the ionization energy of the hydrogen atom. Thus, the dissociation energy of a given rovibrational state is measured with respect to this asymptote, not from the zero-energy continuum. To approximate this asymptotic reference energy, the code computes an analytic estimate:

$$E_{\text{ref}} = -\text{Ry} \cdot \left(\frac{Z_1 Z_3}{n} \right)^2 \cdot \frac{m_1 m_3}{m_1 + m_3},$$

where Z_1 and Z_3 are the charges, and m_1, m_3 are the masses of the two interacting particles (the proton and electron). The principal quantum number n reflects the energy level of the hydrogen-like system; for the ground state, $n = 1$. This formula gives a reasonable approximation for the asymptotic energy of the molecular potential curve in atomic units. For the case of H_2^+ , the result is approximately $E_{\text{ref}} \sim -0.49972783971 \text{ a.u.}$

The total physical energy of a bound state is then recovered from the rescaled eigenvalue ϵ via E [eV] = $\epsilon \cdot E_S - E_{\text{ref}}$. Using this variational approach, we find the following results for eigenvalues and dissociation energies of two rovibrational states:

- For $(\nu = 0, L = 2)$: $\epsilon = -0.59634520549099816537$, $E_{\text{dis}} = -2.6290924577$ eV
- For $(\nu = 1, L = 2)$: $\epsilon = -0.58640363153225673566$, $E_{\text{dis}} = -2.3585684489$ eV

Subtracting the reference energy, these correspond to dissociation energies of approximately

$$E_{\text{dis}}(\nu = 0, L = 2) \approx -0.0966173658 \text{ a.u.}$$

$$E_{\text{dis}}(\nu = 1, L = 2) \approx -0.0866757918 \text{ a.u.}$$

below the asymptotic limit. These values, equivalent to roughly -2.6 eV and -2.3 eV, lie near the bottom of the $1s\sigma_g$ potential well. This confirms that the computed states correspond to low-lying rovibrational levels of H_2^+ . For comparison, I also computed the lowest energy bound state in this potential has a dissociation energy of approximately -2.65069 eV. The close agreement demonstrates that the numerical method accurately reproduces the strong binding characteristic of the ground vibrational manifold.

The dissociation energy difference between the $\nu = 0$ and $\nu = 1$ levels is $\Delta E_{\text{dis}} = 0.270524$ eV. To resolve this energy spacing via two-photon spectroscopy, the required frequency resolution must be on the order of

$$\frac{\Delta E_{\text{dis}}}{2h} \approx \frac{6.54124}{2} \times 10^{13} \text{ Hz} = 3.27062 \times 10^{13} \text{ Hz} = 32.7062 \text{ THz}. \quad (2.4)$$

This sets a target linewidth for the two-photon transition, and highlights the precision needed in the laser frequency stabilization for accurate rovibrational spectroscopy.

I.2 Magnetic and Hyperfine Interactions

Although relativistic effects in this light, three-body system are quantitatively small, their inclusion is essential for achieving the ultra-high precision required in modern spectroscopic experiments. A widely adopted approach for incorporating relativistic corrections in such systems is to begin with the non-relativistic Hamiltonian H^{NR} , which accurately captures the dominant dynamics, and systematically add perturbative corrections arising from relativistic effects.

These corrections are typically divided into spin-independent and spin-dependent contributions. The spin-independent terms, denoted by V^{diag} , primarily account for relativistic kinematic corrections and modifications to the Coulomb interaction. The spin-dependent terms include both the internal spin interactions, V^{spin} , and the interaction with an external magnetic field, V^{mag} . The full Hamiltonian can therefore be written as

$$H = H^{\text{NR}} + V^{\text{diag}} + V^{\text{spin}} + V^{\text{mag}}$$

H₂⁺ Energy Diagram

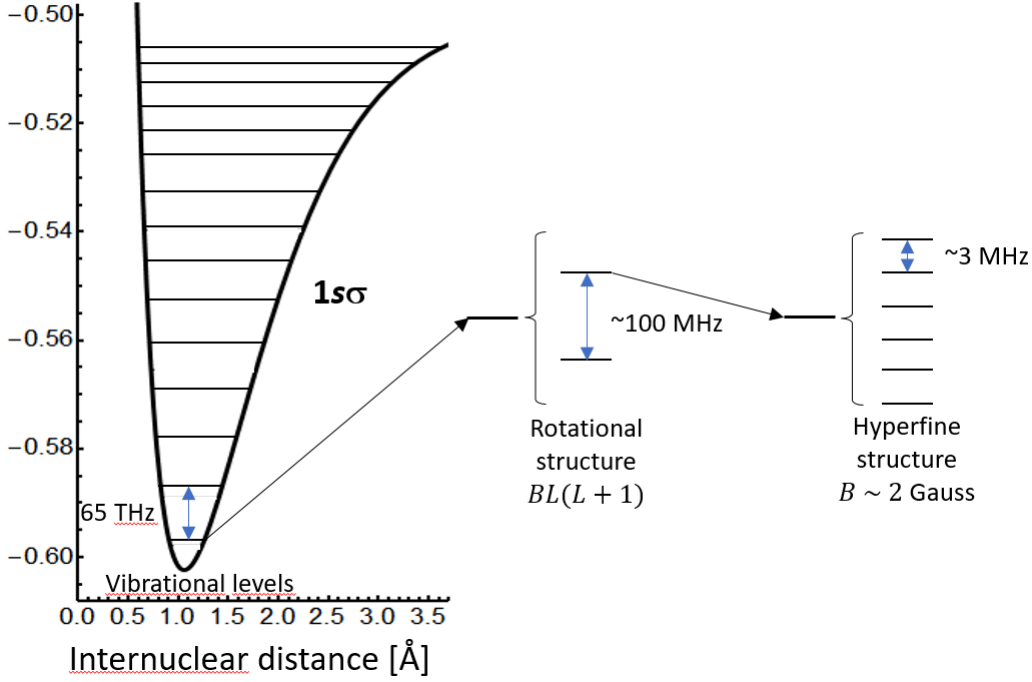


Figure 2.1: Order-of-magnitude diagram of the energy scales relevant in this work. The hyperfine structure lies far below the rovibrational splittings and requires high-precision modeling to resolve.

The leading-order relativistic corrections are given by the Breit-Pauli Hamiltonian, which contributes at order α^2 relative to the non-relativistic energy. We focus on $V^{\text{spin}} + V^{\text{mag}}$. The spin structure of the rovibrational state (ν, L) , where ν and L are the vibrational and total orbital momentum quantum numbers, is computed in first-order perturbation theory using an effective Hamiltonian H_{hfs} , obtained by averaging $V^{\text{spin}} + V^{\text{mag}}$ over the spatial degrees of freedom [6].

For high-precision comparisons, the relevant frequency intervals span a broad range. In this system, transitions correspond to intervals on the order of 65×10^{12} Hz, or approximately 33 Hz in two-photon transitions. These values translate to energies in electron-volts via $E = h\nu$, and corresponding wavelengths can be calculated using $\lambda = \frac{c}{\nu}$.

$$\begin{aligned}
 H_{\text{hfs}} = & b_F(\mathbf{I} \cdot \mathbf{S}_e) + c_e(\mathbf{L} \cdot \mathbf{S}_e) + c_I(\mathbf{L} \cdot \mathbf{I}) \\
 & + \frac{d_1}{(2L-1)(2L+3)} \left(\frac{2}{3} \mathbf{L}^2(\mathbf{I} \cdot \mathbf{S}_e) - [(\mathbf{L} \cdot \mathbf{I})(\mathbf{L} \cdot \mathbf{S}_e) + (\mathbf{L} \cdot \mathbf{S}_e)(\mathbf{L} \cdot \mathbf{I})] \right) \\
 & + \frac{d_2}{(2L-1)(2L+3)} \left(\frac{1}{3} \mathbf{L}^2 \mathbf{I}^2 - \frac{1}{2}(\mathbf{L} \cdot \mathbf{I}) - (\mathbf{L} \cdot \mathbf{I})^2 \right).
 \end{aligned} \tag{2.5}$$

Neglecting relativistic and radiative corrections, the interaction of the H₂⁺ ion with an external magnetic field can be described, to linear order in the field strength, by the Zeeman Hamiltonian:

$$H_Z = g_e \mu_B \mathbf{S}_e \cdot \mathbf{B} - g_p \mu_p \mathbf{I} \cdot \mathbf{B} + \mu_B \mathbf{L}_e \cdot \mathbf{B} - \mu_p (\mathbf{L}_1 + \mathbf{L}_2) \cdot \mathbf{B}. \tag{2.6}$$

The total effective Hamiltonian to be diagonalized is thus composed of the hyperfine structure Hamiltonian and the Zeeman interaction:

$$H = H_{\text{hfs}} + H_Z. \quad (2.7)$$

If $I \neq 0$, the strongest coupling is the spin-spin electron- proton interaction, i.e., the first term in Eq. (2.9). This interaction determines the principal splitting of the rovibrational levels of H_2^+ . With this consideration in mind, the preferable coupling scheme of angular momentum operators is

$$\mathbf{F} = \mathbf{S}_e + \mathbf{I}, \quad \mathbf{J} = \mathbf{L} + \mathbf{F}. \quad (2.8)$$

If the nuclear spin vanishes ($I = 0$), the orbital angular momentum quantum number L is even, and within this coupling scheme the hyperfine Hamiltonian (2.5) simplifies to the spin-orbit coupling form

$$H_{\text{hfs}} = c_e \mathbf{L} \cdot \mathbf{S}_e = \frac{c_e}{2} (\mathbf{J}^2 - \mathbf{L}^2 - \mathbf{S}_e^2). \quad (2.9)$$

For ($I = 0, L = 2$), there are $2L + 1 = 5$ magnetic sublevels of orbital angular momentum, each of which is coupled to a two-level spin-1/2 system, giving $5 \times 2 = 10$ total states. We work in the coupled basis $|v, L, S_e, J, M_J\rangle$, where v is the vibrational quantum number. For each value of J , M_J spans from $-J$ to $+J$ in integer steps.

The basis set used in the following calculations is ordered by increasing total angular momentum \bar{J} , and, for each fixed \bar{J} , by increasing magnetic quantum number M_J , as illustrated below:

$$\begin{aligned} & \{|v, L, S_e = 1/2, J = 3/2, M_J = -3/2\rangle, |v, L, S_e = 1/2, J = 3/2, M_J = -1/2\rangle, \\ & \quad |v, L, S_e = 1/2, J = 3/2, M_J = 1/2\rangle, |v, L, S_e = 1/2, J = 3/2, M_J = 3/2\rangle, \\ & |v, L, S_e = 1/2, J = 5/2, M_J = -5/2\rangle, |v, L, S_e = 1/2, J = 5/2, M_J = -3/2\rangle, \\ & |v, L, S_e = 1/2, J = 5/2, M_J = -1/2\rangle, |v, L, S_e = 1/2, J = 5/2, M_J = 1/2\rangle, \\ & \quad |v, L, S_e = 1/2, J = 5/2, M_J = 3/2\rangle, |v, L, S_e = 1/2, J = 5/2, M_J = 5/2\rangle\}. \end{aligned}$$

I.3 Zeeman Splitting

| L | ν | $J = L - 1/2$ | $J = L + 1/2$ | $\langle \nu, L L_e \nu, L \rangle / \sqrt{2L + 1}$ | $\langle \nu, L L_1 \nu, L \rangle / \sqrt{2L + 1}$ | g_{rot} |
|-----|-------|---------------|---------------|---|---|------------------|
| 2 | 0 | -63.2438 | 42.1625 | 1.069×10^{-4} | 1.22469 | 0.9198 |
| | 1 | -59.3574 | 39.5716 | 1.193×10^{-4} | 1.22469 | 0.9105 |

Table 2.1: Hyperfine splittings (in MHz) and reduced matrix elements of L_e and L_1 (divided by $\sqrt{2L + 1}$) for the rovibrational levels (ν, L) with $L = 2$ and $\nu = 0, 1$ of H_2^+ . The values of $\langle\langle L_{\text{tot}} \rangle\rangle$ are not explicitly listed, but the last column shows the corresponding rotational g factors. Data from [6, 7].

The Hamiltonian H in equation (2.7) is diagonalized using a Mathematica program I developed, following the method described in [19]. Employing the hyperfine coefficients listed in Table 2.1, the full Hamiltonian matrix is constructed by combining contributions from the spin-orbit, rotational, and hyperfine operators: \mathbf{S}_e , \mathbf{L} , and H_{hfs} . Diagonalizing this matrix yields both the energy eigenvalues and corresponding eigenstates. All energies are converted to frequency units via E/h , ensuring direct comparability with spectroscopic measurements. The resulting eigenstates are superpositions of basis states sharing the same magnetic quantum number M_J but differing in total angular momentum J . In particular, the two states with $M_J = \pm 5/2$ remain unmixed, while the remaining eight states appear as linear combinations of the form:

$$|\nu, L, S_e, I, F, \bar{J}, M_J\rangle = C_{5/2} |\nu, L, S_e, J = 5/2, M_J\rangle + C_{3/2} |\nu, L, S_e, J = 3/2, M_J\rangle.$$

To label these mixed states, we define \bar{J} as the J value corresponding to the largest coefficient in magnitude, and M_J remains as a good quantum number. This is because with $\mathbf{B} = B\hat{k}$, rotational symmetry is broken except around the z -axis, so J_z commutes with the Hamiltonian and M_J remains conserved.

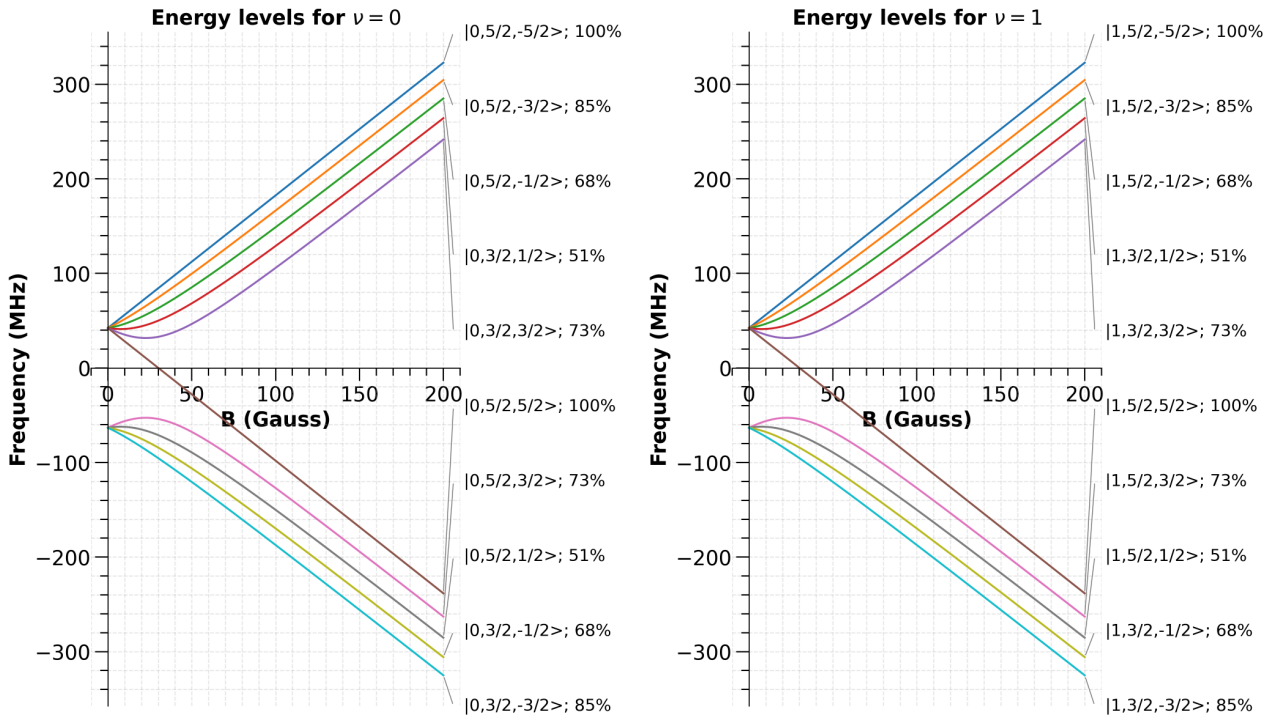


Figure 2.2: Energy levels of the hyperfine states for both rovibrational levels as a function of the applied magnetic field B in the range 0–200 Gauss.

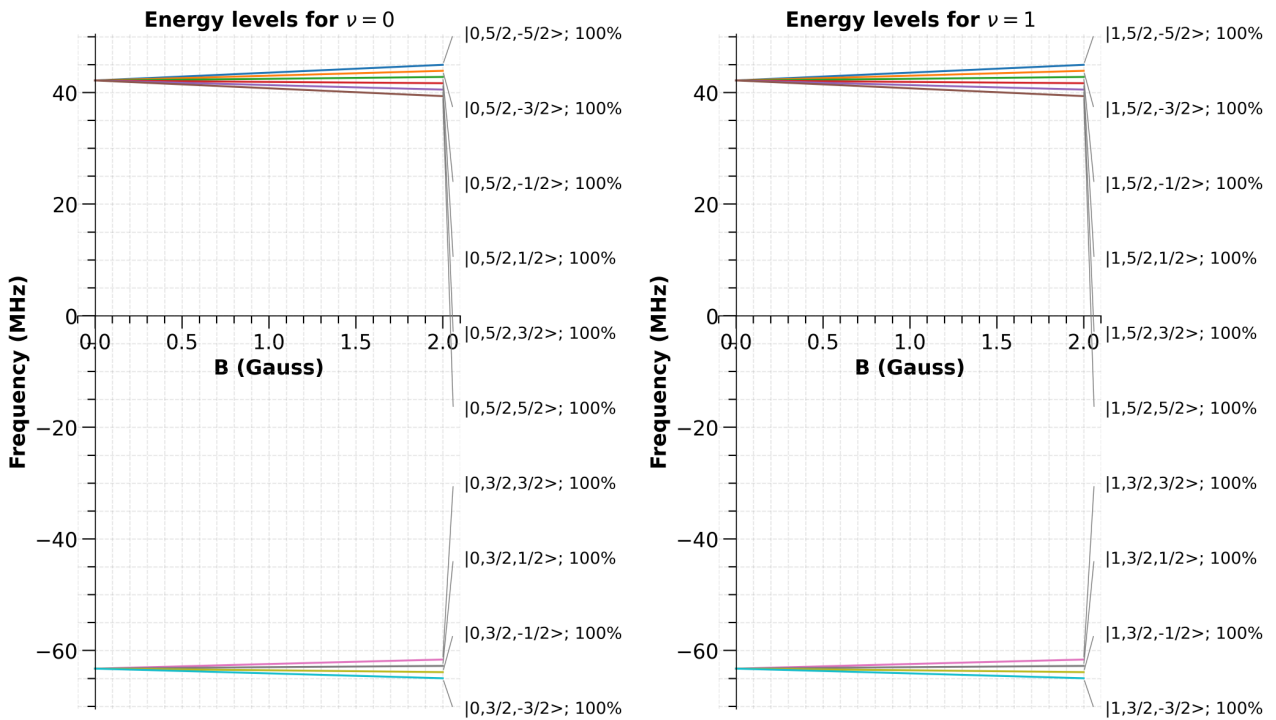


Figure 2.3: Energy levels of the hyperfine states for both rovibrational levels as a function of the applied magnetic field B in the range 0–2 Gauss.

In the range 0–200 Gauss (Figure 2.2), the energy levels exhibit significant curvature as the magnetic field increases. This behavior arises because the electronic Zeeman interaction becomes the dominant term in the Hamiltonian, leading to the progressive decoupling of the orbital angular momentum \mathbf{L} and the electron spin \mathbf{S}_e . As a consequence, J is no longer a good quantum number, and the eigenstates become admixtures of the original $J = 3/2$ and $5/2$ basis states. In the high-field limit, the levels regroup according to the spin projection $S_e = \pm 1/2$, and their energies are primarily determined by the electronic Zeeman effect.

The states with $J = 5/2$, $M = \pm 5/2$ retain a pure character (mixing coefficient 100%) across the entire field range because they correspond to a unique combination of L and S_e . Their energies therefore vary linearly with B , even at high fields. For the other states, the mixing coefficients approach 50% as the field increases, reflecting the transition to the high-field regime where the eigenstates become nearly equal mixtures of the low-field $J = 3/2$ and $5/2$ states.

At low magnetic fields (Figure 2.3), the hyperfine interaction dominates, and the eigenstates remain close to pure J states. The Zeeman effect introduces small linear shifts proportional to B , and the energy splittings are primarily determined by the coupling between \mathbf{L} and \mathbf{S}_e . The mixing coefficients remain near 100%, indicating that the states largely preserve this low-field character.

II Two-Photon Spectroscopy

Two-photon spectroscopy is a powerful tool for high-precision measurements, particularly in systems like H_2^+ where electric dipole transitions are forbidden between certain states due to selection rules. In such cases, transitions proceed via the simultaneous absorption of two photons, described within second-order perturbation theory. A convenient framework for analyzing these transitions is provided by the dressed atom formalism [20], which naturally incorporates essential features such as dynamic Stark shifts. In this formalism, the interaction between the atom and the light field is treated in a way that highlights how these shifts and the two-photon coupling arise from the applied fields.

II.1 Two Photon Operator

The irreducible tensor operator formalism provides a powerful framework for analyzing two-photon transitions between two states $|g\rangle$ and $|e\rangle$, as it enables a straightforward identification of selection rules and simplifies the calculation of transition amplitudes. To describe such transitions in H_2^+ under arbitrary polarization configurations, we begin by introducing the effective two-photon transition operator:

$$Q_{\epsilon_1\epsilon_2} = \mathbf{d} \cdot \epsilon_1 \frac{1}{H - E} \mathbf{d} \cdot \epsilon_2, \quad (2.10)$$

where \mathbf{d} is the electric dipole operator, H is the full atomic Hamiltonian, and E represents the energy of the intermediate virtual states. These virtual states are not real, observable

eigenstates of the system, but rather off-resonant intermediate levels that mediate the two-photon transition via second-order perturbation theory (see Figures 2.4, 2.5, 2.6 for a schematic representation of the role of virtual states).

The irreducible tensor operator formalism provides a powerful framework for analyzing two-photon transitions between two states $|g\rangle$ and $|e\rangle$, as it enables a straightforward identification of selection rules and simplifies the calculation of transition amplitudes. To describe such transitions in H_2^+ under arbitrary polarization configurations, we begin by introducing the effective two-photon transition operator:

$$Q_{\epsilon_1\epsilon_2} = \mathbf{d} \cdot \epsilon_1 \frac{1}{H - E} \mathbf{d} \cdot \epsilon_2, \quad (2.11)$$

where \mathbf{d} is the electric dipole operator, H is the full atomic Hamiltonian, and E represents the energy of the intermediate virtual states. The polarization vectors ϵ_1 and ϵ_2 describe the two excitation field polarizations interacting with the ion.

To account for the indistinguishability of the absorption order, the physical observable involves the symmetrized operator:

$${}^S Q_{\epsilon_1\epsilon_2} = \frac{1}{2} (Q_{\epsilon_1\epsilon_2} + Q_{\epsilon_2\epsilon_1}). \quad (2.12)$$

It is convenient to express both the dipole operator and the polarization vectors in the spherical basis. The components of the dipole operator are then written as d_q , where $q = -1, 0, +1$ corresponds to circularly polarized (σ^- , π , σ^+) transitions. Accordingly, the polarization vectors ϵ_1 , ϵ_2 are replaced by their spherical components q_1 , q_2 , and the operator becomes:

$$Q_{q_1q_2} = d_{q_1} \frac{1}{H - E} d_{q_2}; \quad {}^S Q_{q_1q_2} = \frac{1}{2} (Q_{q_1q_2} + Q_{q_2q_1}) \quad (2.13)$$

The operator $Q_{q_1q_2}$ is formed from the product of two dipole operators. It can be decomposed into irreducible tensor components of rank $k = 0, 1, 2$ using angular momentum coupling:

$$Q_q^{(k)} = \sum_{q_1, q_2} \langle kq | 11q_1q_2 \rangle Q_{q_1q_2}, \quad k = 0, 1, 2. \quad (2.14)$$

where $q = q_1 + q_2$, and $\langle kq | 11q_1q_2 \rangle$ are Clebsch–Gordan coefficients. The inverse relation allows one to re-express the symmetrized two-photon operator in terms of these irreducible components:

$${}^S Q_{q_1q_2} = \sum_{q=-2}^2 a_q^{(2)} Q_q^{(2)} + a_0^{(0)} Q_0^{(0)}. \quad (2.15)$$

where the $a_q^{(k)}$ coefficients are given in Table 2.2.

This decomposition is crucial for determining selection rules, evaluating light shifts, and computing transition matrix elements.

| | σ^- | π | σ^+ |
|------------|---|---|--|
| | $q_1 = -1$ | $q_1 = 0$ | $q_1 = +1$ |
| σ^- | $a_q^{(2)} = \delta_{q,-2}$ | $a_q^{(2)} = \frac{\sqrt{2}}{2}\delta_{q,-1}$ | $a_q^{(2)} = \frac{\sqrt{6}}{6}\delta_{q,0}$ |
| $q_2 = -1$ | $a_0^{(0)} = 0$ | $a_0^{(0)} = 0$ | $a_0^{(0)} = \frac{\sqrt{3}}{3}$ |
| π | $a_q^{(2)} = \frac{\sqrt{2}}{2}\delta_{q,-1}$ | $a_q^{(2)} = \sqrt{\frac{2}{3}}\delta_{q,0}$ | $a_q^{(2)} = \frac{\sqrt{2}}{2}\delta_{q,1}$ |
| $q_2 = 0$ | $a_0^{(0)} = 0$ | $a_0^{(0)} = -\frac{\sqrt{3}}{3}$ | $a_0^{(0)} = 0$ |
| σ^+ | $a_q^{(2)} = \frac{\sqrt{6}}{6}\delta_{q,0}$ | $a_q^{(2)} = \frac{\sqrt{2}}{2}\delta_{q,1}$ | $a_q^{(2)} = \delta_{q,2}$ |
| $q_2 = +1$ | $a_0^{(0)} = \frac{\sqrt{3}}{3}$ | $a_0^{(0)} = 0$ | $a_0^{(0)} = 0$ |

Table 2.2: Values of the coefficient $a_q^{(k)}$ for all combinations of the standard polarizations.

II.2 Transition Matrix Elements

The central quantity in both two-photon transition probabilities and Raman Rabi frequencies is the matrix element of the symmetrized two-photon operator ${}^S Q_{q_1 q_2}$ between coupled hyperfine states. Using the Wigner–Eckart theorem, the matrix element between the initial state $|\phi\rangle = |\nu, L, S_e, I, F, J, M_J\rangle \equiv |gJ, M_J\rangle$ and final state $|\psi\rangle = |\nu', L', S_e, I', F, J', M'_J\rangle \equiv |eJ', M'_J\rangle$ can be expressed as

$$\langle\phi|^S Q_{q_1 q_2} |\psi\rangle = \sum_k a_q^{(k)} \langle J' M'_J | k q J M_J \rangle \frac{\langle gJ || Q^{(k)} || eJ' \rangle}{\sqrt{2J+1}}, \quad (2.16)$$

where the reduced matrix element can be separated into a purely angular part and a rovibrational matrix element [21]:

$$\begin{aligned} \langle g, J || Q^{(k)} || e, J' \rangle &= \delta_{I, I'} (-1)^{J'+L+F+k} \sqrt{2J+1} \sqrt{2J'+1} \\ &\times \left\{ \begin{array}{ccc} L & k & L' \\ J' & F & J \end{array} \right\} \langle \nu, L || Q^{(k)} || \nu', L' \rangle \end{aligned} \quad (2.17)$$

The symmetrized two-photon operator ${}^S Q_{q_1 q_2}$ can drive both rovibrational transitions, where the molecule moves from ν to $\nu' \neq \nu$, and Raman (intra-rovibrational) transitions, where $\nu' = \nu$ but internal hyperfine states change.

Rovibrational transitions govern the population transfer between different vibrational levels and determine the absolute excitation strengths. These processes occur in an incoherent regime, where individual excitation events are not phase-related and coherence between quantum states is not maintained. In contrast, Raman transitions describe coherent coupling between hyperfine states within the same vibrational level, enabling controlled state evolution characterized by Rabi oscillations. While the incoherent regime is relevant for estimating transition rates and population redistribution across vibrational levels, the coherent regime is essential for manipulating superpositions and driving precise dynamics within a single rovibrational manifold.

II.2.1 Two-Photon Transition Probability

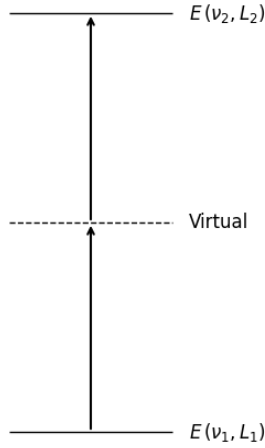


Figure 2.4: Two-photon rovibrational transition at resonance.

For a laser of intensity I , we define the two-photon transition probability per unit time P between an initial hyperfine state $|\phi\rangle$ and a final state $|\psi\rangle$ (with different rovibrational quantum numbers $\nu \neq \nu'$) as [6]:

$$P = \left(\frac{4\pi a_0^3}{\hbar c} \right)^2 \frac{4}{\Gamma_f} I^2 \left| \langle \phi |^S Q_{q_1 q_2} | \psi \rangle \right|^2, \quad (2.18)$$

where a_0 is the Bohr radius and Γ_f is the instrumental width of the transition. The instrumental width Γ_f represents the effective linewidth of the observed transition. It sets the frequency window within which the transition can be efficiently driven.

The transition probability P is directly proportional to the square of the two-photon matrix element $\langle \phi |^S Q_{q_1 q_2} | \psi \rangle$, which encodes the coupling strength between the two states via virtual intermediate levels. This formulation allows us to identify favorable quantum numbers and polarization configurations for driving efficient population transfer between rovibrational states. Moreover, P reflects the interplay between rotational-vibrational dynamics and angular momentum selection rules as described by second-order perturbation theory.

II.2.2 Two-Photon Rabi Frequency

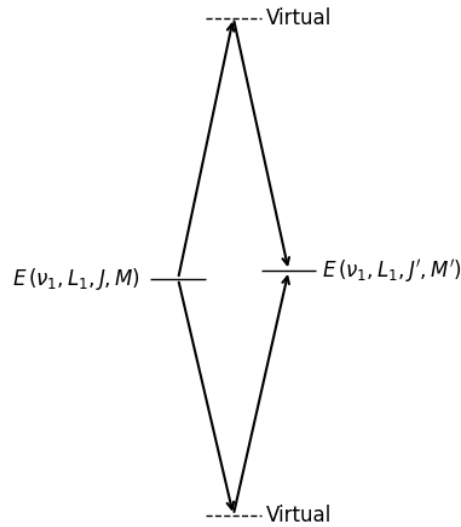


Figure 2.5: Raman transition occurring within the same rovibrational state and involving different hyperfine sublevels.

When the two-photon detuning is set near zero within the same rovibrational level ($\nu = \nu'$), the system undergoes coherent Rabi oscillations between two hyperfine states $|g\rangle$ and $|e\rangle$. We note that the generalized Rabi frequency can be written as

$$\Omega_{ge} = \frac{4\pi a_0^3 I}{hc} |\langle g |^S Q_{q_1 q_2} | e \rangle|, \quad (2.19)$$

correcting the prefactor compared to the expression in [5].

The Rabi frequency characterizes the strength of coherent coupling between quantum states under continuous laser driving. Its computation is restricted to transitions within the same vibrational level because in this regime, energy conservation implies negligible detuning. This allows one to treat the dynamics in terms of population oscillations governed by Ω .

II.2.3 Polarizability and Light Shifts

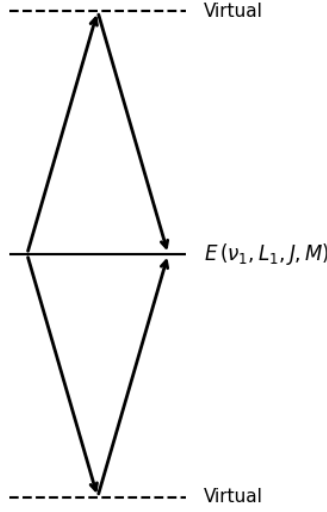


Figure 2.6: ac Stark shifts experienced by a hyperfine level under two-photon illumination.

The same matrix formalism used to compute transition amplitudes allows us to determine the dynamic polarizability of a hyperfine state $|n\rangle$ under two-photon illumination at angular frequency ω .

In a spherical tensor basis, the dynamic polarizability becomes

$$\alpha^n(\omega) = -4\pi a_0^3 \sum_{q_1, q_2} \epsilon_{q_1} \epsilon_{q_2} \langle n |^S Q_{q_1 q_2} (E_n + \hbar\omega) + {}^S Q_{q_1 q_2} (E_n - \hbar\omega) | n \rangle. \quad (2.20)$$

Due to selection rules, only terms with $q_1 + q_2 = 0$ contribute to the expectation value $\langle n |^S Q_{q_1 q_2} | n \rangle$, which ensures angular momentum conservation in the two-photon interaction. Consequently, the relevant polarization combinations are:

- $(q_1, q_2) = (0, 0)$ corresponding to π - π light,
- $(q_1, q_2) = (+1, -1)$ and $(-1, +1)$, corresponding to $\sigma^+ - \sigma^-$ and $\sigma^- - \sigma^+$ combinations.

This implies that circular polarization pairs of opposite handedness, such as (σ^+, σ^-) and (σ^-, σ^+) , contribute to the polarizability, as long as the electric field contains both components. Conversely, mixed combinations like (π, σ^\pm) or (σ^\pm, π) , where $q_1 + q_2 \neq 0$, do not contribute due to orthogonality. Thus, for an electric field with polarization components $\vec{\epsilon} = \epsilon_0 \hat{e}_0 + \epsilon_+ \hat{e}_{+1} + \epsilon_- \hat{e}_{-1}$, the light shift of state $|n\rangle$ becomes

$$\Delta E_n = -\frac{1}{4} \left(|\epsilon_0|^2 \langle n |^S Q_{\pi\pi} | n \rangle + \epsilon_+ \epsilon_-^* \langle n |^S Q_{\sigma^+\sigma^-} | n \rangle + \epsilon_+^* \epsilon_- \langle n |^S Q_{\sigma^-\sigma^+} | n \rangle \right). \quad (2.21)$$

Finally, the differential light shift of a two-photon transition between states $|g\rangle$ and $|e\rangle$, evaluated at $\omega_{ge} = \frac{E_e - E_g}{2\hbar}$, is given by

$$\Delta E^{ge} = -\frac{1}{4} \frac{\Delta \alpha_\epsilon^{ge}}{c}, \quad \Delta \alpha_\epsilon^{ge} = \alpha_\epsilon^e(\omega_{ge}) - \alpha_\epsilon^g(\omega_{ge}). \quad (2.22)$$

Chapter 3

Methods and Results

I Transition Energies

For $I = 0$, the nuclear spin terms vanish, and the Zeeman Hamiltonian (2.6) simplifies to $H_Z \approx g_e \mu_B \mathbf{S}_e \cdot \mathbf{B} + \mu_B \mathbf{L} \cdot \mathbf{B}$. Together with the hyperfine interaction $H_{\text{hfs}} = c_e \mathbf{L} \cdot \mathbf{S}_e$, the total Hamiltonian (2.7) governs the energy shifts as a function of the magnetic field $\Delta E(B) = E_e(B) - E_g(B)$. Following the approach of [19], I computed the eigenvalues and eigenstates for the $|\nu = 0, L = 2\rangle$ and $|\nu = 1, L = 2\rangle$ levels using *Mathematica*. By applying the appropriate selection rules, I extracted the corresponding two-photon transition energies, given by $\Delta E(B)/2$.

In the low-field regime (Figure 3.2), the hyperfine interaction dominates. The eigenstates are well described by the quantum numbers J and M_J , and the Zeeman interaction introduces small perturbative corrections:

$$E(B) \approx E_0 + \gamma B M_J,$$

where γ is an effective coupling constant that involves the action of \mathbf{L} and \mathbf{S}_e . Selection rules impose $M'_J = M_J + q$, so the transition energy varies approximately as $\Delta E(B) \propto (M'_J - M_J)B$. Thus, for $q = q_1 + q_2 \neq 0$, the transition energy shows a linear dependence on B . In contrast, for $q = 0$ transitions, where $M'_J = M_J$, the linear terms cancel in the energy difference, and the shift is dominated by higher-order contributions (typically quadratic in B) $\Delta E(B) \approx \Delta E(0) + \alpha B^2$.

In the high-field regime (Figure 3.1), the Zeeman interaction becomes the dominant term. The magnetic field effectively decouples \mathbf{L} and \mathbf{S}_e , and the energies are primarily determined by their independent contributions:

$$E(B) \approx E_0 + g_e \mu_B \langle \mathbf{S}_e \rangle B + \mu_B \langle \mathbf{L} \rangle B + (\text{small corrections from hyperfine interaction}).$$

$\langle \mathbf{S}_e \rangle$ and $\langle \mathbf{L} \rangle$ are the effective contributions from spin and orbital angular momentum in the states. The hyperfine interaction still contributes as a perturbation, introducing residual coupling between levels with similar energy. This residual coupling induces level repulsion and leads to nonlinear bending in the energy curves as a function of the magnetic field.

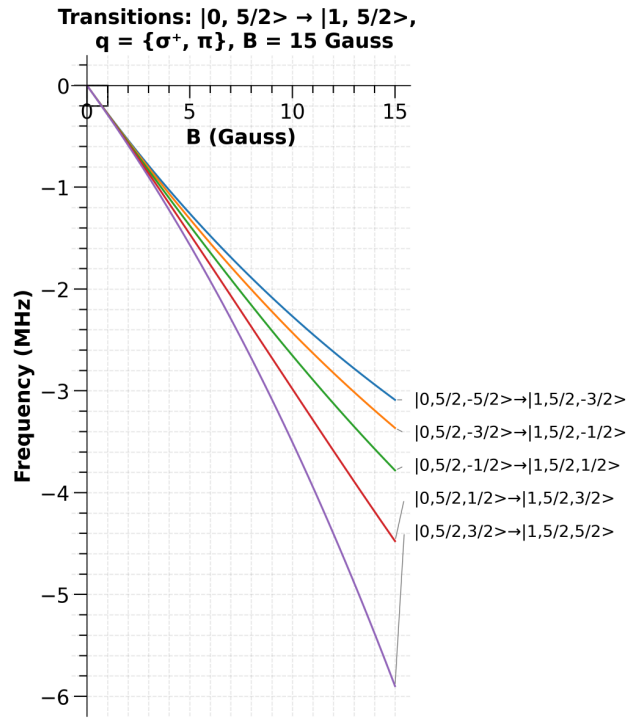
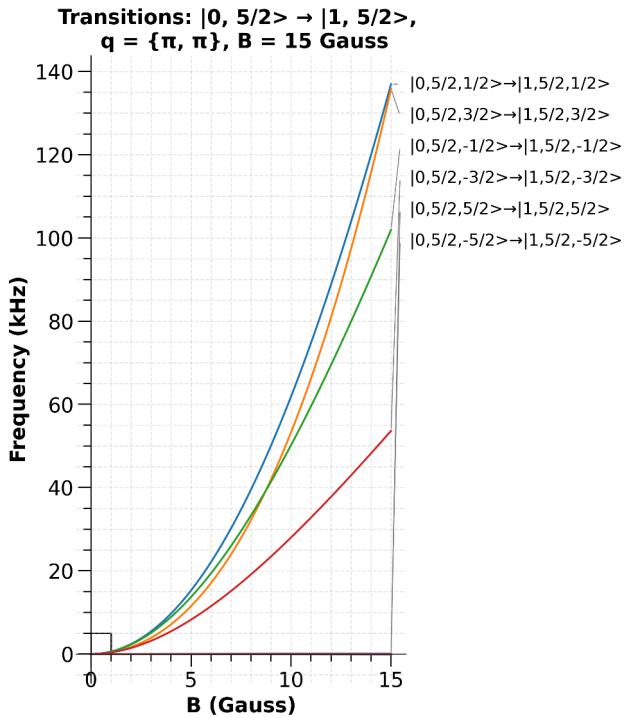
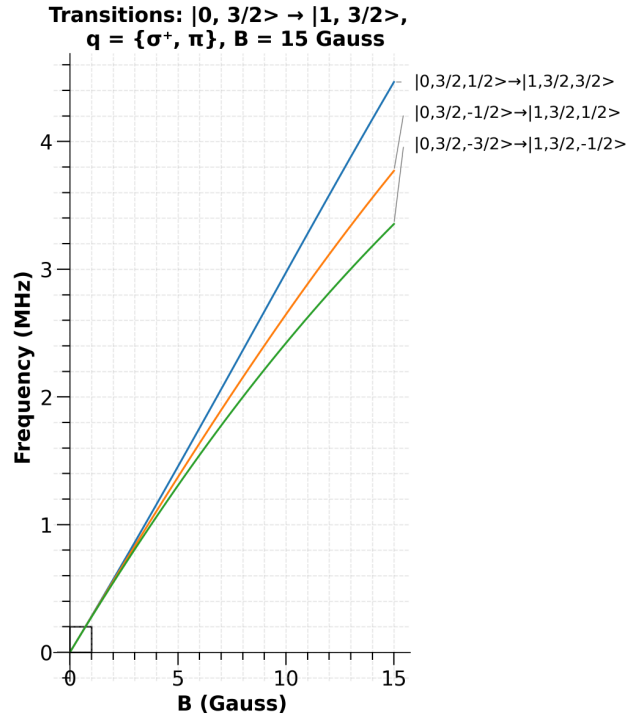
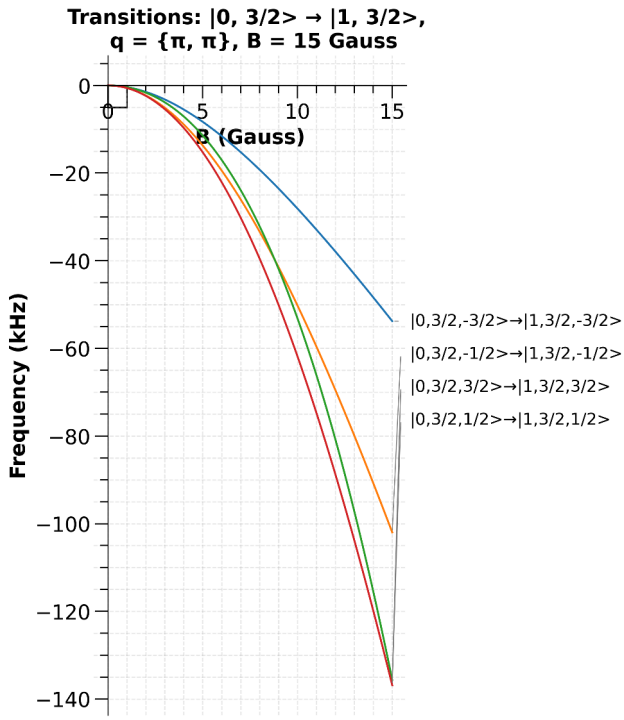


Figure 3.1: Calculated two-photon transition energies as a function of magnetic field (0–15 G) for $|\bar{J}, M_J\rangle \rightarrow |\bar{J}, M'_J\rangle$ transitions, shown for polarization components $q = 0$ (left) and $q = 1$ (right). For $q = 1$, the transitions exhibit a dominant linear Zeeman splitting, while for $q = 0$, nonlinear behavior persists, especially in states with strong hyperfine mixing. The region highlighted by a square corresponds to the low-field regime explored in detail in Figure 3.2.

Note: The y -axis units differ among the panels and must be read carefully.

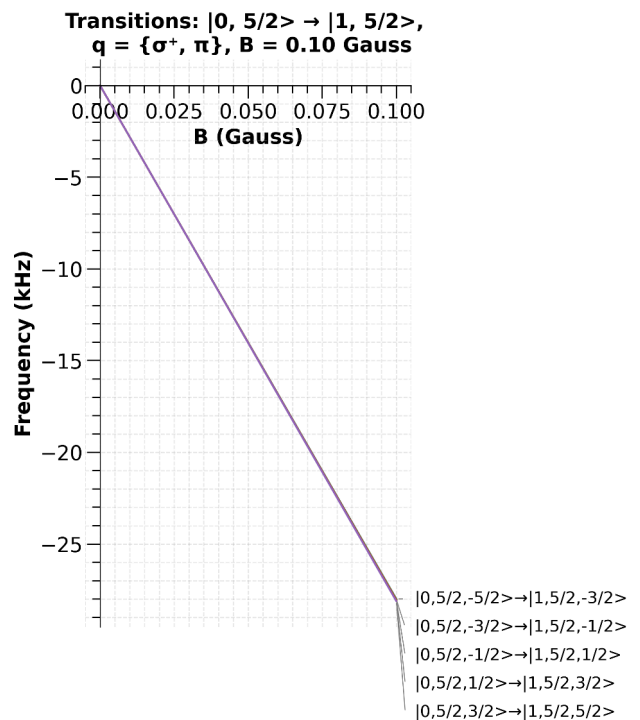
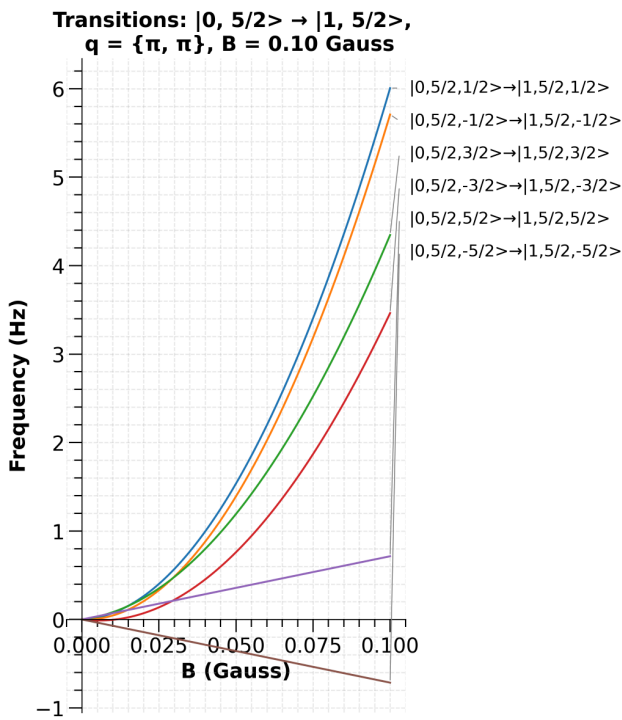
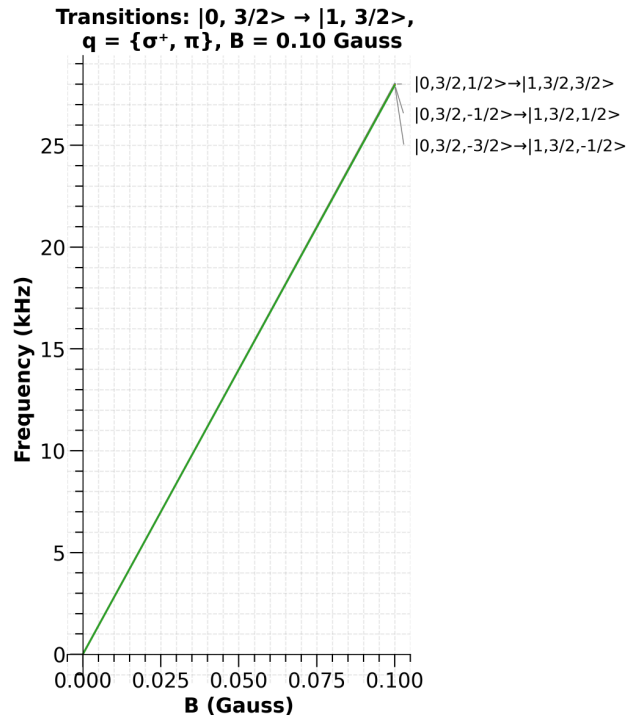
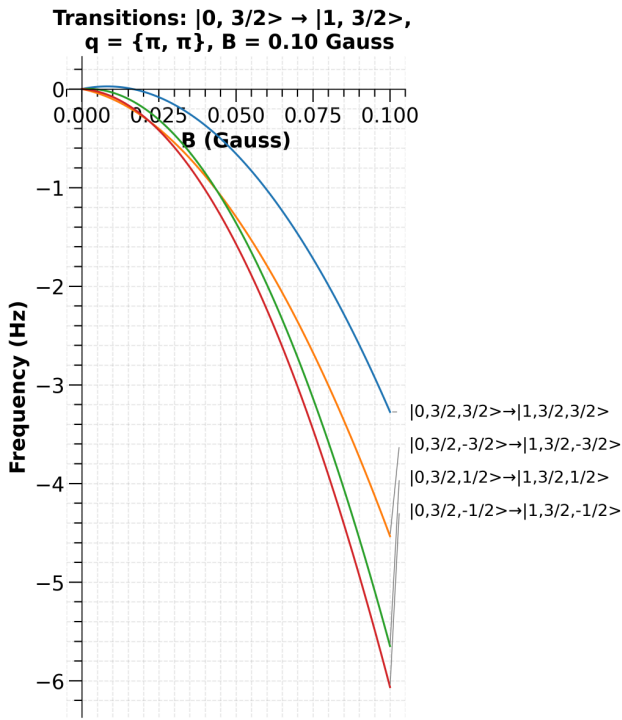


Figure 3.2: Zoomed-in view of the low-field regime (0–0.1 G) corresponding to the boxed region in Figure 3.1. In this regime, the hyperfine interaction dominates. For $q = 1$, the Zeeman shifts are small but linear, while for $q = 0$, the transition energies exhibit predominantly nonlinear (quadratic) dependence on B , characteristic of mixed states. Note: The y -axis units differ among the panels and must be read carefully.

As a result, both $q = 0$ and $q \neq 0$ transitions exhibit nonlinearities at high magnetic fields. For $q \neq 0$ transitions, the transition energies retain a strong linear dependence on B , with nonlinearity appearing only as a small correction at larger fields. In contrast, for $q = 0$ transitions (where the leading linear contributions to the energy difference cancel due to $\Delta M_J = 0$) the nonlinear behavior stemming from hyperfine-induced level mixing becomes more pronounced.

This distinction is clearly reflected in our numerical results: for $q = 0$ transitions, the energy shifts remain extremely small even at nonzero fields, with values $\lesssim 6$ kHz at $B = 0.1$ G. In contrast, $q = 1$ transitions exhibit shifts on the order of 30 kHz at the same field strength, nearly 5000 times larger (see Figure 3.2). This stark difference highlights the dominant role of linear Zeeman shifts in $\Delta M_J \neq 0$ transitions and underscores the sensitivity of $q = 0$ transitions to second-order (and higher) perturbative effects arising from residual hyperfine couplings.

II Spinless Matrix Elements

As discussed in Section I and Appendix A, the resonance energies of few-body quantum systems, such as three-body Coulombic systems, are obtained by transforming the Schrödinger equation into a generalized matrix eigenvalue problem, which is then solved numerically. The code used in this work relies on basis functions optimized for rapid convergence, and experience with this code suggests that basis sizes in the range of $N = 550$ – 900 are sufficient for achieving the required accuracy. For the present calculations, I used these standard values, which provide a good balance between computational cost and precision. Tests with slightly larger N confirmed that the results did not change significantly, indicating that the chosen basis size is adequate for transition probability calculations.

The reduced matrix elements $\langle vL||Q^{(k)}||v'L' \rangle$ are computed numerically by summing over contributions from intermediate states with angular momentum $L'' = L - 1, L, L + 1$. These terms are evaluated using the dipole operator

$$d = \sum Z_a R_a,$$

where the sum runs over all particles a (e.g., the nuclei and electron), with Z_a the charge number and R_a the position of particle a . The three contributions are:

$$a_- = - \sum_{v''} \frac{\langle vL|d|v''L-1\rangle \langle v''L-1|d|v'L'\rangle}{(2L+1)(2L'-1)(\omega - E_{v''L-1})}, \quad (3.1)$$

$$a_+ = - \sum_{v''} \frac{\langle vL|d|v''L+1\rangle \langle v''L+1|d|v'L'\rangle}{(2L+1)(2L'+1)(\omega - E_{v''L+1})}, \quad (3.2)$$

$$a_0 = \sum_{v''} \frac{\langle vL|d|v''L\rangle \langle v''L|d|v'L'\rangle}{(2L+1)(2L'+1)(\omega - E_{v''L})}, \quad (3.3)$$

where $E_{v''L''}$ is the energy of the intermediate state $|v''L''\rangle$, and ω is the photon angular frequency. For two-photon transitions, the photon energy is $\omega = (E_{vL} - E_{v'L'})/2$. In our calculations, we consistently use the reduced matrix elements $\frac{\langle vL|Q^{(k)}||v'L' \rangle}{\sqrt{2L+1}}$ rather than the bare

$\langle \nu L | Q^{(k)} | \nu' L' \rangle$. The scalar ($k = 0$) and quadrupole ($k = 2$) components of the operator are given by [5]:

$$\frac{\langle \nu L | Q^{(0)} | \nu' L' \rangle}{\sqrt{2L+1}} = -\frac{\sqrt{3}}{3} (a_- + a_0 + a_+), \quad (3.4)$$

$$\frac{\langle \nu L | Q^{(2)} | \nu' L' \rangle}{\sqrt{2L+1}} = -\frac{1}{\sqrt{6}} \sqrt{(2L+3)(2L-1)L(L+1)} \times \left[\frac{a_-}{L(2L-1)} - \frac{a_0}{L(L+1)} + \frac{a_+}{(2L+3)(L+1)} \right]. \quad (3.5)$$

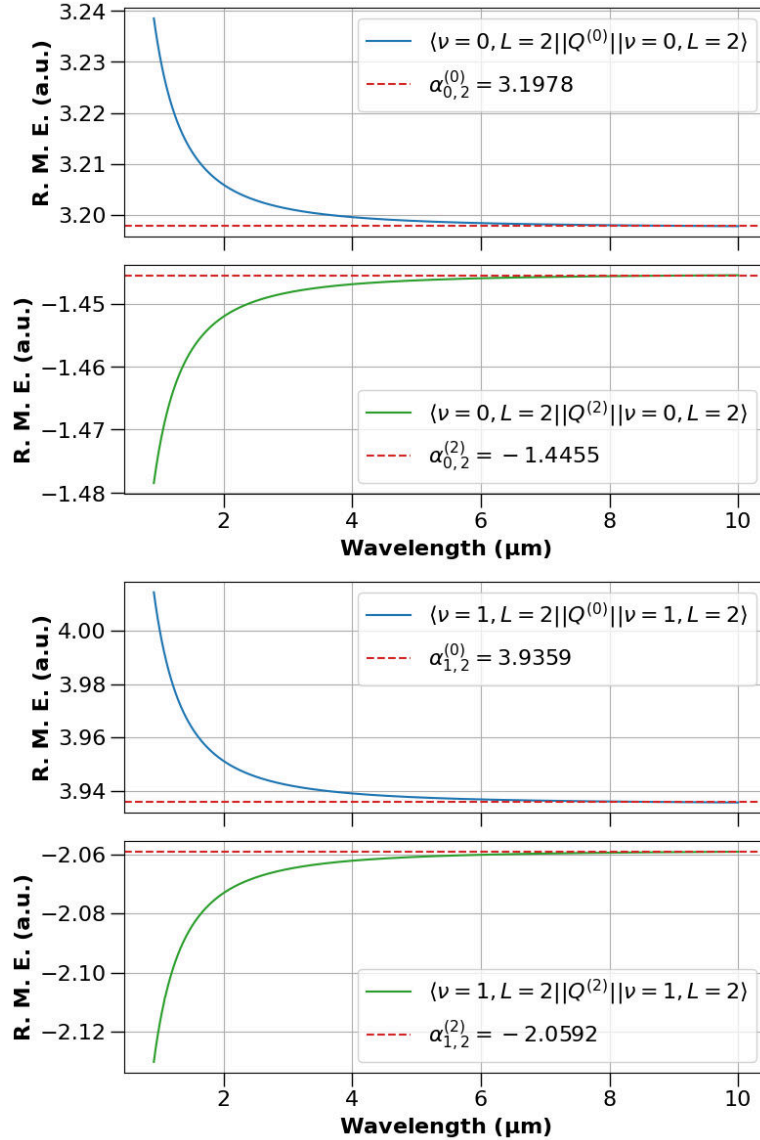


Figure 3.3: Reduced Matrix Elements $\langle \nu L | Q^{(k)} | \nu' L' \rangle \equiv \langle \nu L | Q^{(k)} | \nu' L' \rangle / (\sqrt{2L+1})$ for the Raman Rabi frequency calculations for the states $|\nu=0, L=2\rangle$ (top) and $|\nu=1, L=2\rangle$ (bottom) across different wavelengths. The red-dotted line represents the static polarizability ($\lambda \rightarrow \infty$) found in [5].

Since the two-photon transition between rovibrational states is a resonant process, we adopt a resonant wavelength of $9.15\ \mu\text{m}$ to compute the corresponding matrix elements. Our results for the reduced two-photon matrix elements are $\langle 0\ 2||Q^{(0)}||1\ 2\rangle = -0.547278$, $\langle 0\ 2||Q^{(2)}||1\ 2\rangle = 0.422419$. In comparison, Jean-Philippe Karr reports in Ref. [5] the values $\langle 0\ 2||Q^{(0)}||1\ 2\rangle = -0.4239$, $\langle 0\ 2||Q^{(2)}||1\ 2\rangle = 0.3119$.

Although the polarisabilities computed for each rovibrational level match perfectly with those in Ref. [5] as seen in Figure 3.3, the values of the two-photon matrix elements show a discrepancy. Since both results were obtained using the same computational framework, this difference likely arises from differences in numerical precision, integration parameters, or implementation details in the evaluation of the two-photon operator. For instance, differences in the choice of energy reference point, level of convergence, or intermediate state truncation could impact the matrix elements even if the underlying physics and code are equivalent.

III Two-Photon Probabilities per Unit Time

Using a Mathematica code that I developed to compute the two-photon operator matrix elements, based on the formalism outlined in Section I.3 and Eqs.(2.16) and (2.17), I analyzed two-photon rovibrational transitions in H_2^+ . My calculations focus on initial states with $\nu = 0$, examining the dependence on magnetic quantum numbers \bar{J} and M_J , as well as on various photon polarization combinations (q_1, q_2) . The transition wavelength is set to $9.15, \mu\text{m}$, and I varied the external magnetic field from 0 to 1 Gauss. For clarity, I present the results using the notation $|\bar{J}, M_J\rangle \rightarrow |\bar{J}', M_J'\rangle$, which is shorthand for $|\nu = 0, \bar{J}, M_J\rangle \rightarrow |\nu = 1, \bar{J}', M_J'\rangle$.

It's possible to normalize the comparison across all transitions under the assumption of equal light intensity and being in resonant regime according to Equation (2.18), thus we can directly interpret the squared matrix elements $|\langle^S Q_{q_1 q_2}\rangle|^2$ as relative transition probabilities. These values reflect the efficiency of driving rovibrational population transfer, modulated by the overlap of angular momentum states, dipole selection rules, and the symmetry of the polarization combination.

III.1 General trends

The following figures show the calculated spectra for different polarization configurations. Each set of four panels corresponds to a specific polarization pair, organized as follows: left column, $B = 0$ Gauss; right column, $B = 1$ Gauss; top row, transitions with $|3/2, M_J\rangle \rightarrow |3/2, M_J'\rangle$, bottom row, transitions with $|5/2, M_J\rangle \rightarrow |5/2, M_J'\rangle$. Please note that the labels within each panel are local and are not meant to be compared directly between panels.

The following behaviors reflect the two-photon selection rule $\Delta M = q_1 + q_2$, where q_i is the angular momentum of photon i (0 for π , ± 1 for σ^\pm).

- (π, π) polarizations consistently yield the highest transition probabilities. This is expected, as π polarizations favor $\Delta M = 0$ transitions, where selection rules and Clebsch-Gordan coefficients strongly support no change in magnetic quantum number. Extremal magnetic sublevels ($|M| = \bar{J}$) exhibit the highest $|\langle^S Q_{q_1 q_2}\rangle|^2$, reaching up to ~ 0.3 a.u. for $\bar{J} = 5/2$ and $\gtrsim 0.15$ a.u. for $\bar{J} = 3/2$. Transitions involving central $|M|$ decrease below 0.1 a.u. but remain significant compared to polarizations where $q_1 + q_2 \neq 0$.
- (σ^\pm, σ^\mp) also support $\Delta M = 0$ transitions but via different intermediate-state couplings, leading to smaller probabilities than (π, π) through an 'opposite' behaviour since transitions involving central $|M|$ dominates this time.
- (π, σ^\pm) or (σ^\pm, π) combinations lead to weak $|\langle^S Q_{q_1 q_2}\rangle|^2$, as they mix $\Delta M = 0$ and $\Delta M = \pm 1$ contributions, which couple less efficiently resulting in weaker angular momentum couplings. We have $|\langle^S Q_{q_1 q_2}\rangle|^2$ around 0.02 a.u. - 0.038 a.u. for outer-inner sublevel transitions while opposite M transitions are strongly suppressed.
- (σ^\pm, σ^\pm) produce small but noticeable $|\langle^S Q_{q_1 q_2}\rangle|^2$ for $\Delta M = \pm 2$ transitions, in agreement with angular momentum selection rules. We reach values around 0.04 a.u. for $\bar{J} = 3/2$ and 0.068 a.u. for $\bar{J} = 5/2$.

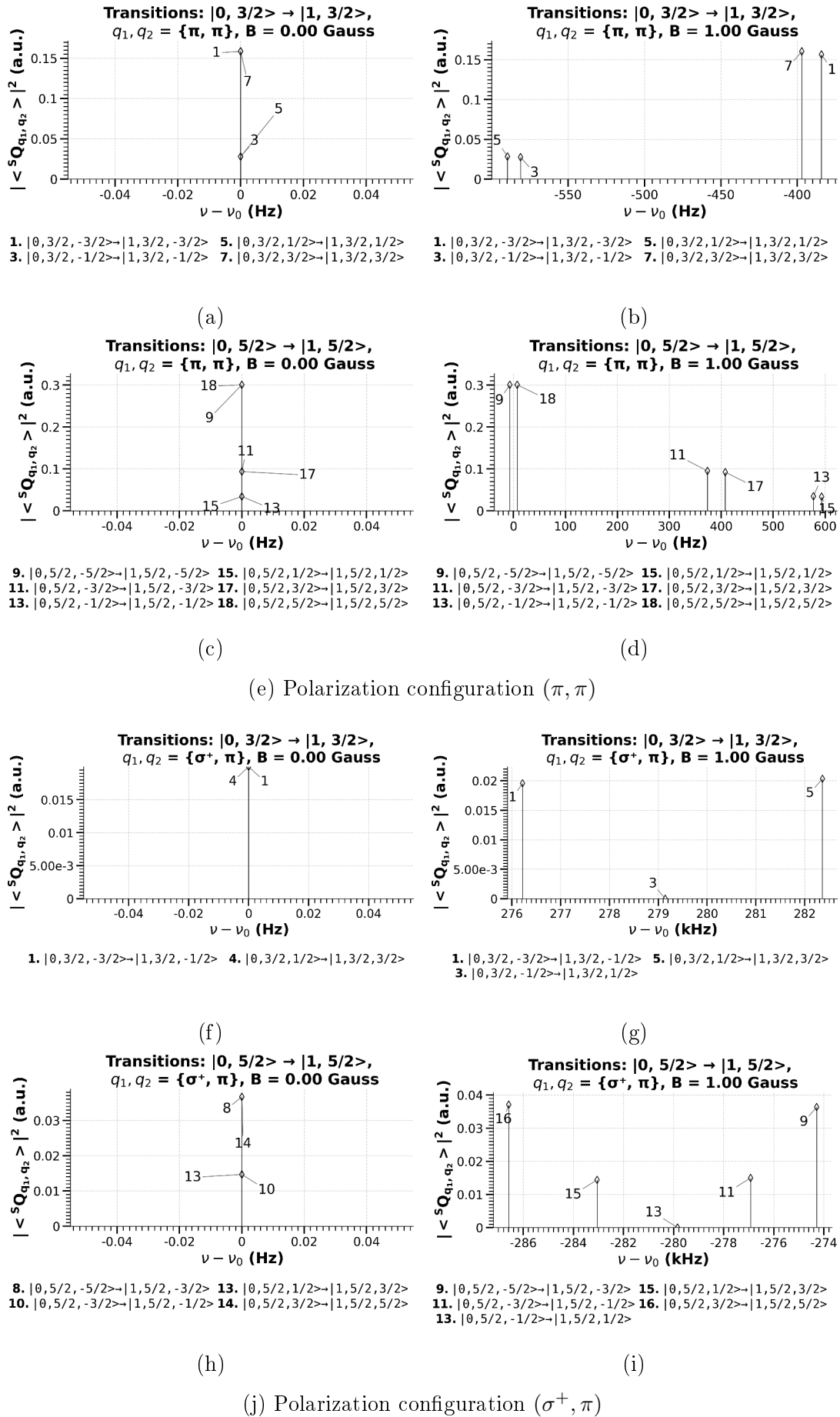


Figure 3.4: Two Photon Rovibrational Transitions for two polarization configurations. Each subpanel shows the corresponding magnetic field strength and transition type. Local labels are not comparable across panels.

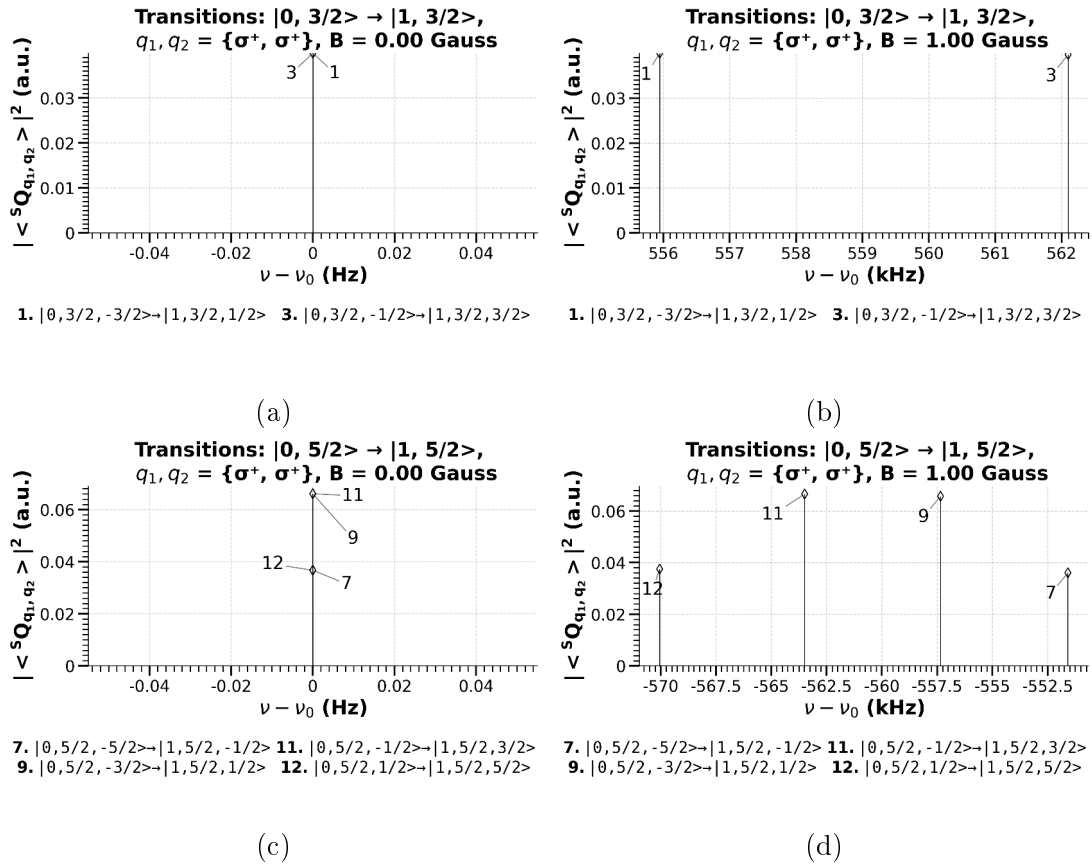


Figure 3.5: Two Photon Rovibrational Transitions for (σ^+, σ^+) polarization configuration. Each subpanel shows the corresponding magnetic field strength and transition type. Local labels are not comparable across panels.

III.2 Behavior for $\bar{J} = 3/2$

For (π, π) , the most probable transitions are those that conserve M , specifically $|3/2, \pm 3/2\rangle \rightarrow |3/2, \pm 3/2\rangle$, with $|\langle^S Q_{q_1 q_2}\rangle|^2$ around 0.16 a.u. for magnetic fields below 1 Gauss. The energy ordering of these transitions reverses at $B \approx 0.8$ Gauss due to the nonlinear Zeeman splitting of the sublevels under these polarisations (Figure 3.4 (a) and (b)). The complementary (σ^\pm, σ^\mp) configurations yield lower $|\langle^S Q_{q_1 q_2}\rangle|^2$, approximately 0.07 a.u. for $|3/2, \pm 1/2\rangle \rightarrow |3/2, \pm 1/2\rangle$ and about 0.03 a.u. for $|3/2, \pm 3/2\rangle \rightarrow |3/2, \pm 3/2\rangle$.

For mixed polarizations (π, σ^\pm) , transitions that change $|M|$ by one unit, such as $|3/2, -3/2\rangle \rightarrow |3/2, -1/2\rangle$ or $|3/2, 1/2\rangle \rightarrow |3/2, 3/2\rangle$, are the dominant ones but occur with $|\langle^S Q_{q_1 q_2}\rangle|^2$ around 0.02 a.u. Opposite- M transitions like $|3/2, -1/2\rangle \rightarrow |3/2, 1/2\rangle$ are strongly suppressed, with $|\langle^S Q_{q_1 q_2}\rangle|^2$ below 10^{-3} a.u. (Figure 3.4 (f) and (g)). Same-helicity circular polarizations (σ^\pm, σ^\pm) produce small but measurable $\Delta M = \pm 2$ transitions, with $|\langle^S Q_{q_1 q_2}\rangle|^2 \gtrsim 0.04$ a.u. (Figure 3.5 (a) and (b)).

III.3 Behavior for $\bar{J} = 5/2$

For (π, π) , the strongest transitions are $|5/2, \pm 5/2\rangle \rightarrow |5/2, \pm 5/2\rangle$, with $|\langle^S Q_{q_1 q_2}\rangle|^2$ near 0.3 a.u. Transitions involving lower $|M|$ values are weaker, with $|\langle^S Q_{q_1 q_2}\rangle|^2 \sim 0.1$ a.u. for $M = \pm 3/2$ and $|\langle^S Q_{q_1 q_2}\rangle|^2 \sim 0.05$ for $M = \pm 1/2$ (Figure 3.4 (c) and (d)). In contrast, the (σ^\pm, σ^\mp)

configurations favor transitions with lower $|M|$: $|5/2, \pm 1/2\rangle \rightarrow |5/2, \pm 1/2\rangle$ reach $|\langle^S Q_{q_1 q_2}\rangle|^2$ around 0.1 a.u., while $|5/2, \pm 3/2\rangle \rightarrow |5/2, \pm 3/2\rangle$ give about 0.08 a.u. The $|\langle^S Q_{q_1 q_2}\rangle|^2$ for $M = \pm 5/2$ drop to about 0.04 a.u.

For (π, σ^\pm) , the $\Delta M = \pm 1$ transitions remain modest for external transitions, typically with $|\langle^S Q_{q_1 q_2}\rangle|^2 \sim 0.037$ a.u., then they decrease to around 0.015 a.u. for more inner transitions and negligible for $|M| = 1/2$ (Figure 3.4 (h) and (i)). Same-helicity circular polarizations (σ^\pm, σ^\pm) result in small but detectable $\Delta M = \pm 2$ transitions, with $|\langle^S Q_{q_1 q_2}\rangle|^2$ around 0.068 a.u. for paths involving both $M = \pm 1/2$ and $\pm 3/2$ (Figure 3.5 (c) and (d)).

III.4 Magnetic Field dependence

The magnetic field modifies both the energy levels and the structure of the eigenstates through Zeeman splitting (as discussed in Section I.3), which in turn affects two-photon coupling strengths. This influence is most evident in the reversal of transition energy orderings for $q = 0$ and in the gradual redistribution of $|\langle^S Q_{q_1 q_2}\rangle|^2$ among different M levels as the field increases (Figure 3.4).

IV Light Shifts in Two-Photon Hyperfine Transitions

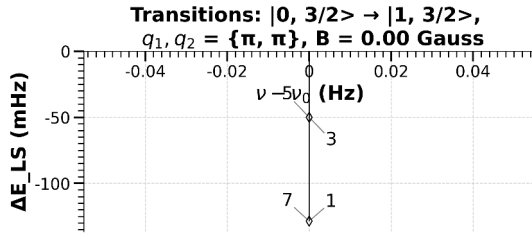
With the same Mathematica code that I developed for computing the two-photon operator matrix elements—based on the formalism outlined in Section I.3 and Eqs. (2.16), (2.17), and (2.22)—I analyzed the AC Stark shifts (light-induced energy shifts) associated with two-photon transitions between hyperfine sublevels of the H_2^+ molecular ion, for magnetic fields ranging from 0 to 1 Gauss. The transition photon wavelength is set to $9.15 \mu\text{m}$. The results are expressed using the notation $|\bar{J}, M_J\rangle \rightarrow |\bar{J}', M_J'\rangle$ (a shorthand for $|\nu = 0, \bar{J}, M_J\rangle \rightarrow |\nu = 1, \bar{J}', M_J'\rangle$), with a particular emphasis on the influence of different laser polarization combinations and angular momentum projections on the observed shifts.

For polarization combinations $(q_1, q_2) = (\pi, \pi), (\sigma^\pm, \pi), (\pi, \sigma^\pm)$, the polarizability is assumed to be dominated by the $\pi\pi$ channel. For simplicity, we attribute the entire laser intensity to this channel $I = 0.1 \text{ W/mm}^2$. This assumption highlights the relative behavior of the various polarization configurations rather than their absolute values. In a real experimental setup, each laser beam has its own intensity, and the total two-photon coupling depends on the product of the corresponding field amplitudes. Adjusting to realistic intensity distributions would therefore amount to a straightforward rescaling of the computed results, without altering the trends reported here.

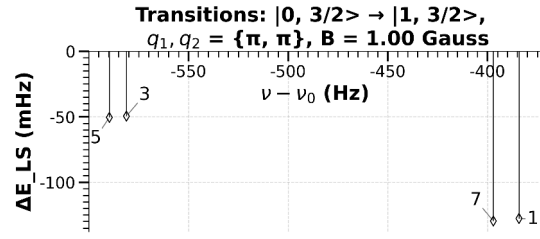
For mixed circular polarizations (σ^\pm, σ^\mp) , both permutations contribute symmetrically, and the laser intensity is divided equally between the (σ^+, σ^-) and (σ^-, σ^+) components ($I/2$ for each one). Transitions with $q_1 + q_2 = 0$ (i.e., $\Delta M_J = 0$) induce scalar light shifts and are therefore excluded from the differential light shift analysis.

IV.1 General Trends

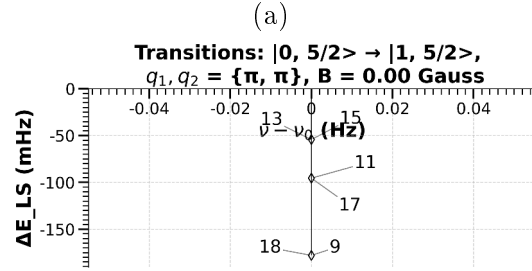
The following figures show the calculated spectra for different polarization configurations. Each set of four panels corresponds to a specific polarization pair, organized as follows: left column, $B = 0$ Gauss; right column, $B = 1$ Gauss; top row, transitions with $|3/2, M_J\rangle \rightarrow |3/2, M_J'\rangle$, bottom row, transitions with $|5/2, M_J\rangle \rightarrow |5/2, M_J'\rangle$. Please note that the labels within each panel are local and are not meant to be compared directly between panels.



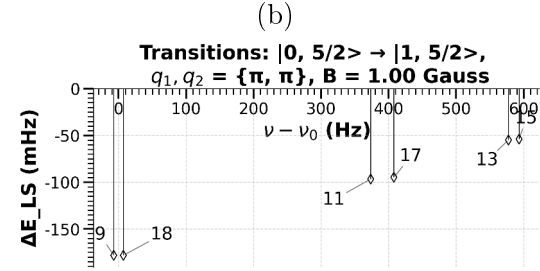
1. $|0, 3/2, -3/2\rangle \rightarrow |1, 3/2, -3/2\rangle$ 5. $|0, 3/2, 1/2\rangle \rightarrow |1, 3/2, 1/2\rangle$
 3. $|0, 3/2, -1/2\rangle \rightarrow |1, 3/2, -1/2\rangle$ 7. $|0, 3/2, 3/2\rangle \rightarrow |1, 3/2, 3/2\rangle$



1. $|0, 3/2, -3/2\rangle \rightarrow |1, 3/2, -3/2\rangle$ 5. $|0, 3/2, 1/2\rangle \rightarrow |1, 3/2, 1/2\rangle$
 3. $|0, 3/2, -1/2\rangle \rightarrow |1, 3/2, -1/2\rangle$ 7. $|0, 3/2, 3/2\rangle \rightarrow |1, 3/2, 3/2\rangle$



9. $|0, 5/2, -5/2\rangle \rightarrow |1, 5/2, -5/2\rangle$ 15. $|0, 5/2, 1/2\rangle \rightarrow |1, 5/2, 1/2\rangle$
 11. $|0, 5/2, -3/2\rangle \rightarrow |1, 5/2, -3/2\rangle$ 17. $|0, 5/2, 3/2\rangle \rightarrow |1, 5/2, 3/2\rangle$
 13. $|0, 5/2, -1/2\rangle \rightarrow |1, 5/2, -1/2\rangle$ 18. $|0, 5/2, 5/2\rangle \rightarrow |1, 5/2, 5/2\rangle$

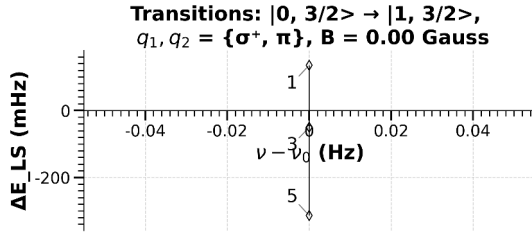


9. $|0, 5/2, -5/2\rangle \rightarrow |1, 5/2, -5/2\rangle$ 15. $|0, 5/2, 1/2\rangle \rightarrow |1, 5/2, 1/2\rangle$
 11. $|0, 5/2, -3/2\rangle \rightarrow |1, 5/2, -3/2\rangle$ 17. $|0, 5/2, 3/2\rangle \rightarrow |1, 5/2, 3/2\rangle$
 13. $|0, 5/2, -1/2\rangle \rightarrow |1, 5/2, -1/2\rangle$ 18. $|0, 5/2, 5/2\rangle \rightarrow |1, 5/2, 5/2\rangle$

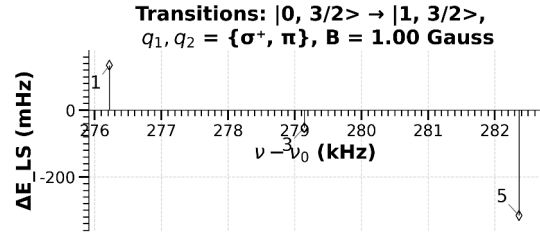
(c)

(d)

(e) Polarization configuration (π, π)



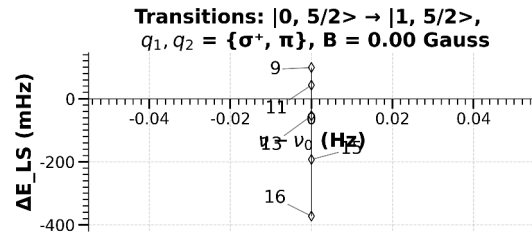
1. $|0, 3/2, -3/2\rangle \rightarrow |1, 3/2, -1/2\rangle$ 5. $|0, 3/2, 1/2\rangle \rightarrow |1, 3/2, 3/2\rangle$
 3. $|0, 3/2, -1/2\rangle \rightarrow |1, 3/2, 1/2\rangle$



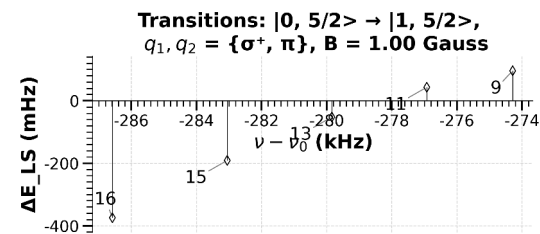
1. $|0, 3/2, -3/2\rangle \rightarrow |1, 3/2, -1/2\rangle$ 5. $|0, 3/2, 1/2\rangle \rightarrow |1, 3/2, 3/2\rangle$
 3. $|0, 3/2, -1/2\rangle \rightarrow |1, 3/2, 1/2\rangle$

(f)

(g)



9. $|0, 5/2, -5/2\rangle \rightarrow |1, 5/2, -3/2\rangle$ 15. $|0, 5/2, 1/2\rangle \rightarrow |1, 5/2, 3/2\rangle$
 11. $|0, 5/2, -3/2\rangle \rightarrow |1, 5/2, -1/2\rangle$ 16. $|0, 5/2, 3/2\rangle \rightarrow |1, 5/2, 5/2\rangle$
 13. $|0, 5/2, -1/2\rangle \rightarrow |1, 5/2, 1/2\rangle$



9. $|0, 5/2, -5/2\rangle \rightarrow |1, 5/2, -3/2\rangle$ 15. $|0, 5/2, 1/2\rangle \rightarrow |1, 5/2, 3/2\rangle$
 11. $|0, 5/2, -3/2\rangle \rightarrow |1, 5/2, -1/2\rangle$ 16. $|0, 5/2, 3/2\rangle \rightarrow |1, 5/2, 5/2\rangle$
 13. $|0, 5/2, -1/2\rangle \rightarrow |1, 5/2, 1/2\rangle$

(h)

(i)

(j) Polarization configuration (σ^+, π)

Figure 3.6: Two-photon light shifts for two polarization configurations. Each subpanel shows the corresponding magnetic field strength and transition type. Local labels are not comparable across panels.

- (π, π) : This configuration allows only $\Delta M_J = 0$ transitions. The observed light shifts are strictly negative, reflecting a scalar-dominated polarizability. The magnitude increases with $|M_J|$, in agreement with the enhanced coupling of stretched states in tensor polarizability interactions.
- (σ^\pm, σ^\mp) : Diagonal transitions are again favored, but here the light shifts are positive. Interestingly, the magnitude is largest for lower $|M_J|$, indicating that tensorial components dominate and their angular dependence favors central Zeeman sublevels.
- (π, σ^\pm) or (σ^\pm, π) : These mixed polarization cases allow $\Delta M_J = \pm 1$ transitions and exhibit both positive and negative light shifts. The shift direction depends on the sign of M_J and the circular polarization's handedness, revealing asymmetries associated with angular momentum transfer and the interference between vector and tensor components.

IV.2 Behavior for $\bar{J} = 3/2$

Under purely longitudinal light (π, π) , the light shifts are negative and increase in magnitude with $|M_J|$. The transition involving $|M_J| = 3/2$ is more strongly shifted than that involving $|M_J| = 1/2$, as expected from the enhanced coupling of stretched states to intermediate levels through electric dipole interactions (Figure 3.6 (a) and (b)). This monotonic trend is consistent with scalar and tensor polarizability effects. For the complementary symmetrized circular polarizations (σ^+, σ^-) are applied, the light shifts become positive. The trend reverses: the $|M_J| = 1/2$ sublevel experiences the largest shift, while the $|M_J| = 3/2$ sublevel is less affected. This behavior suggests the presence of a dominant tensorial interaction whose angular momentum structure favors lower $|M_J|$ states under circular polarizations.

For mixed polarization combinations such as (π, σ^+) , we observe that transitions of the type $|3/2, -3/2\rangle \rightarrow |3/2, -1/2\rangle$ exhibit positive light shifts, whereas their counterparts at the opposite end of the Zeeman ladder, such as $|3/2, 1/2\rangle \rightarrow |3/2, 3/2\rangle$, produce negative shifts (Figure 3.6 (f) and (g)). A similar pattern is found for (π, σ^-) polarization, with the roles of $M_J \leftrightarrow -M_J$ interchanged, illustrating a mirror symmetry under magnetic quantum number inversion. The transition involving $|M_J| = 1/2$, namely $|3/2, -1/2\rangle \rightarrow |3/2, 1/2\rangle$, also results in a negative shift for both cases and is the weakest among them

IV.3 Behavior for $\bar{J} = 5/2$

As in the $\bar{J} = 3/2$ case, (π, π) transitions show exclusively negative shifts that grows nonlinearly and symmetrically in magnitude with increasing $|M_J|$. The strongest shift occurs for the $|M_J| = 5/2$ sublevel, and the smallest for $|M_J| = 1/2$ (Figure 3.6 (c) and (d)). The polarizability in this configuration contains strong scalar and tensor components that preferentially couple stretched states more strongly. Under (σ^+, σ^-) polarization, the behavior is reversed: the largest positive light shift appears for $|M_J| = 1/2$, while the magnitude decreases for $|M_J| = 3/2$ and becomes smallest for $|M_J| = 5/2$. This reversal highlights how the tensor structure of the light shift depends strongly on the polarization geometry and the angular momentum structure of the states involved.

Mixed polarization cases (π, σ^\pm) or (σ^\pm, π) yield shifts that are both positive and negative, depending on the specific transition. For instance, for σ^+ transitions like $|5/2, 3/2\rangle \rightarrow |5/2, 5/2\rangle$ and $|5/2, 1/2\rangle \rightarrow |5/2, 3/2\rangle$ yield negative shifts (decreasing in magnitude in this order), while $|5/2, -3/2\rangle \rightarrow |5/2, -1/2\rangle$ and $|5/2, -5/2\rangle \rightarrow |5/2, -3/2\rangle$ transitions yield positive shifts (increasing in magnitude in this order) (Figure 3.6 (h) and (i)). A similar pattern is found for (π, σ^-) polarization, with the roles of $M_J \leftrightarrow -M_J$ interchanged, illustrating the same mirror symmetry under magnetic quantum number inversion. These transitions are $\Delta M_J = \pm 1$ and their sensitivity to both M_J and the polarization direction confirm that vector components contribute to the light shift and can interfere either constructively or destructively with scalar and tensor parts.

IV.4 Magnetic Field Dependence

For (π, π) transitions, the light shifts remain approximately constant as the magnetic field is varied from $B = 0$ to 1 Gauss. This robustness is expected for $\Delta M_J = 0$ transitions where the intermediate state structure remains largely unaffected by linear Zeeman shifts.

By contrast, transitions under (π, σ^\pm) or (σ^\pm, π) exhibit a mild but observable B -field dependence. For instance, the shift for $|5/2, -1/2\rangle \rightarrow |5/2, -3/2\rangle$ slightly increases with B , while the shift for $|5/2, +3/2\rangle \rightarrow |5/2, +1/2\rangle$ decreases. This behavior arises from the magnetic-field-induced mixing of the hyperfine sublevels, which modifies the angular momentum composition of the states involved. In the Wigner–Eckart formalism, this manifests as a B -dependent redistribution of the transition strengths via the Clebsch–Gordan coefficients and tensor components of the polarizability operator, rather than from any significant change in the energy denominators of the virtual states

Such behavior emphasizes the importance of carefully selecting polarization configurations and field strengths in precision spectroscopy experiments, where differential light shifts can significantly affect measurement accuracy.

V Raman Rabi Frequencies

Building upon the same Mathematica implementation developed for the two-photon operator matrix elements (Section I.3), I extended the calculations to analyze two-photon Raman transitions within the rovibrational ground state ($\nu = 0$) of H_2^+ according to (2.19). Here, the focus is on the behavior of the Rabi frequencies Ω as functions of the magnetic sublevel quantum numbers (\bar{J}, M_J) , polarization combinations (q_1, q_2) , and external magnetic field strengths ranging from 0 to 1 Gauss.

In this section, I consider a representative laser frequency, where the Raman matrix elements $\langle n ||^S Q^{(k)}(E) || n \rangle$ have been computed as a function of the photon energy (see Figure 3.3). Since the Raman transition probability and the associated Rabi frequency depend on the detuning from intermediate virtual states, the choice of the laser wavelength is not unique and can be optimized.

The laser intensity is fixed at $I = 0.1 \text{ W/mm}^2$, and the results for Ω presented below are computed for $\lambda = 1 \mu\text{m}$. The trends discussed are representative of this wavelength, although quantitative values would scale with λ according to the corresponding transition matrix elements. Transitions are labeled using the notation $|\bar{J}, M_J\rangle \rightarrow |\bar{J}', M_J'\rangle$, shorthand for $|\nu = 0, \bar{J}, M_J\rangle \rightarrow |\nu = 0, \bar{J}', M_J'\rangle$.

V.1 General Trends

The following figures show the calculated spectra for different polarization configurations. Each set of four panels corresponds to a specific polarization pair, organized as follows: left column, $B = 0$ Gauss; right column, $B = 1$ Gauss; top row, transitions with $|3/2, M_J\rangle \rightarrow |3/2, M_J'\rangle$, bottom row, transitions with $|5/2, M_J\rangle \rightarrow |5/2, M_J'\rangle$. Please note that the labels within each panel are local and are not meant to be compared directly between panels.

The overall structure follows similar trends observed in two-photon rovibrational transitions. Each polarization combination excites transitions with characteristic angular momentum selection rules, reflected in the distribution and magnitude of the Rabi frequencies.

- (π, σ^\pm) or (σ^\pm, π) : These mixed polarizations allow $\Delta M = \pm 1$ transitions, generally yielding weaker Rabi frequencies. Typical values lie in the range $\Omega \sim 0.46 \text{ Hz} - 0.64 \text{ Hz}$ for outer-to-inner sublevel transitions (e.g., $|\bar{J}, -3/2\rangle \rightarrow |\bar{J}, -1/2\rangle$), while opposite- M transitions (e.g., $|\bar{J}, -1/2\rangle \rightarrow |\bar{J}, 1/2\rangle$) are strongly suppressed, with $\Omega \lesssim 0.01 \text{ Hz}$.
- (σ^\pm, σ^\pm) : These enable $\Delta M = \pm 2$ transitions. Despite the higher angular momentum transfer, Rabi frequencies remain measurable, reaching values around 0.66 Hz for $\bar{J} = 3/2$ and up to 0.85 Hz for $\bar{J} = 5/2$. The Rabi frequencies of these transitions show little or no dependence on the magnetic field.

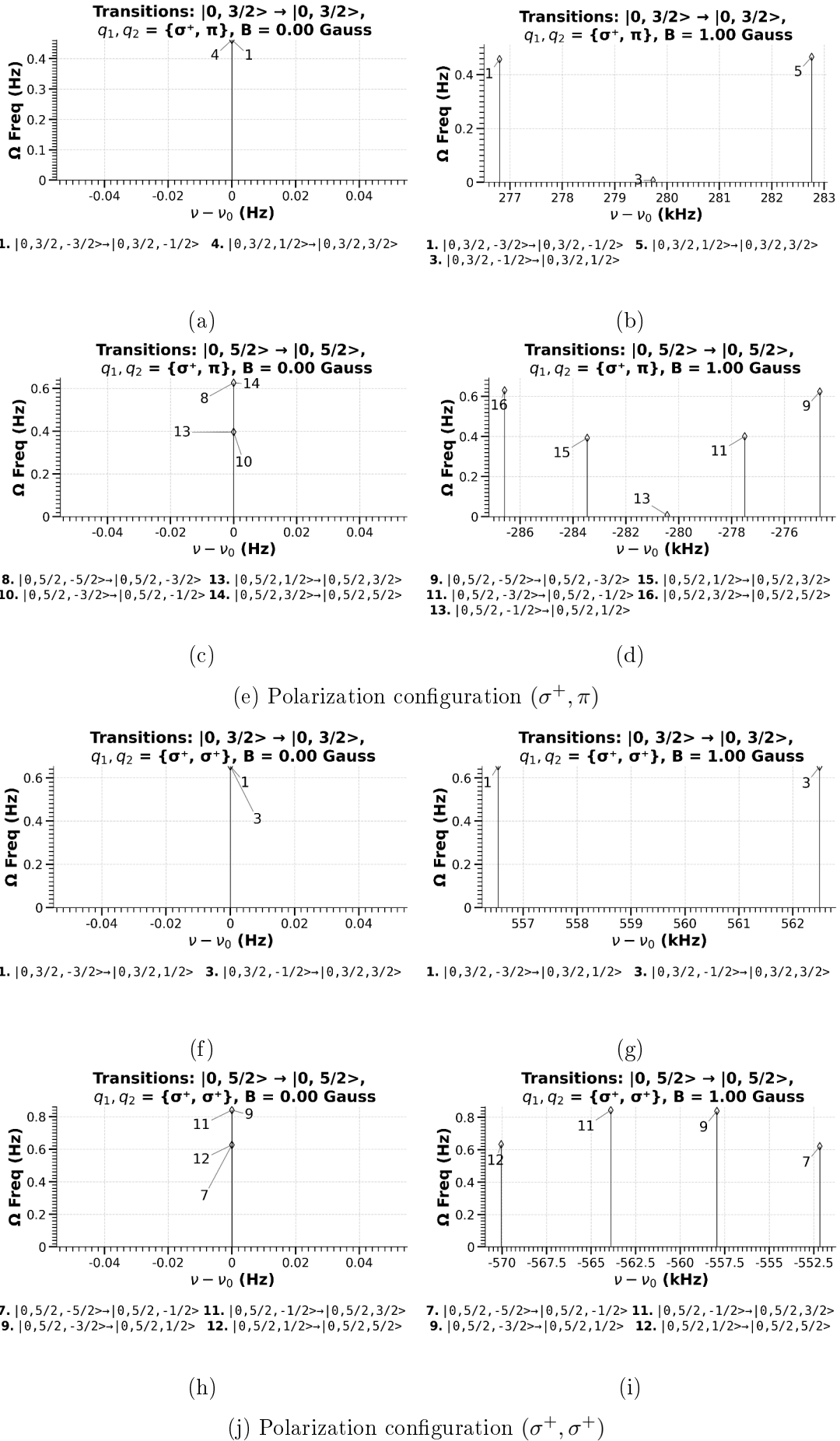


Figure 3.7: Raman Rabi Frequencies for two polarization configurations. Each subpanel shows the corresponding magnetic field strength and transition type. Local labels are not comparable across panels.

V.2 Behavior for $\bar{J} = 3/2$

In the mixed (π, σ^\pm) configurations, transitions that change $|M|$ by 1 (e.g., $|3/2, -3/2\rangle \rightarrow |3/2, -1/2\rangle$ and $|3/2, 1/2\rangle \rightarrow |3/2, 3/2\rangle$) yield $\Omega \sim 0.465$ Hz. Transitions between opposite sublevels (e.g., $|3/2, -1/2\rangle \rightarrow |3/2, 1/2\rangle$) are strongly suppressed, with $\Omega \lesssim 0.01$ Hz, although they exhibit a small increase with B (Figure (3.7) (a) and (b)).

For (σ^\pm, σ^\pm) , $\Delta M = \pm 2$ transitions such as $|3/2, -3/2\rangle \rightarrow |3/2, 1/2\rangle$ or $|3/2, 3/2\rangle \rightarrow |3/2, -1/2\rangle$ produce Rabi frequencies around $\Omega \sim 0.66$ Hz, with no noticeable field dependence (Figure (3.7) (f) and (g)).

V.3 Behavior for $\bar{J} = 5/2$

In the (π, σ^\pm) or (σ^\pm, π) cases, transitions such as $|5/2, |M_J| = 3/2\rangle \leftrightarrow |5/2, |M_J| = 5/2\rangle$ and $|5/2, |M_J| = 1/2\rangle \leftrightarrow |5/2, |M_J| = 3/2\rangle$ show Ω values 0.4 Hz and 0.66 Hz respectively. Opposite- M transitions remain suppressed with $\Omega \lesssim 0.01$ Hz (Figure (3.7) (c) and (d)).

For (σ^\pm, σ^\pm) , $\Delta M = \pm 2$ transitions are robust across all field strengths, with Rabi frequencies between 0.63 Hz and 0.85 Hz, depending on the specific pair of initial and final states (Figure (3.7) (h) and (i)).

V.4 Magnetic Field Dependence

The external magnetic field modifies the Rabi frequencies primarily through Zeeman-induced mixing of the hyperfine sublevels, which alters the angular momentum structure and polarization-dependent couplings. For (π, π) transitions involving extremal magnetic sublevels, this mixing slightly enhances the two-photon matrix elements, leading to a modest increase in Ω . In contrast, transitions involving central sublevels, especially under (σ^\pm, σ^\mp) or (σ^\pm, π) , remain weakly allowed due to symmetry constraints, but still show a small growth in Ω (up to ~ 0.01 Hz at $B = 1$ Gauss) because of the redistribution of transition strength among M_J levels. This behavior is therefore attributed to field-induced mixing and interference effects in the tensor components of the two-photon operator, rather than improved resonance conditions.

VI Light Shifts in Raman Transitions

I applied again the light-shift formalism to analyze the AC Stark shifts (light-induced energy shifts) associated with two-photon Raman transitions between hyperfine sublevels within the vibrational ground state ($v = 0$) of H_2^+ , for magnetic fields ranging from 0 to 1 Gauss. The calculations were performed for a representative photon wavelength of $\lambda = 9.15 \mu\text{m}$, with transitions denoted as $|\bar{J}, M_J\rangle \rightarrow |\bar{J}', M_J'\rangle$, shorthand for $|0, \bar{J}, M_J\rangle \rightarrow |0, \bar{J}', M_J'\rangle$.

For polarization combinations $(q_1, q_2) = (\pi, \pi), (\sigma^\pm, \pi), (\pi, \sigma^\pm)$, the polarizability is dominated by the $\pi\pi$ channel. To simplify the analysis, I assigned the entire laser intensity $I = 0.1 \text{ W/mm}^2$ to this channel. This choice is intended to highlight relative behaviors across polarization configurations; in practice, each laser beam has its own intensity, and the two-photon coupling scales with the product of their field amplitudes. Adjusting to realistic intensity distributions would therefore correspond to a simple rescaling of the computed results.

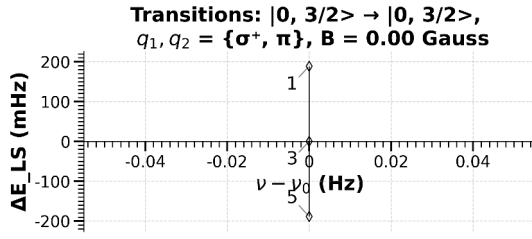
For mixed circular polarizations (σ^\pm, σ^\mp) , both permutations contribute equally, and the laser intensity is divided as $I/2$ between the (σ^+, σ^-) and (σ^-, σ^+) components. Transitions with $q_1 + q_2 = 0$ (i.e., $\Delta M_J = 0$) result in purely scalar light shifts and are excluded from the present discussion, as they do not affect the differential transition frequencies.

VI.1 General Trends

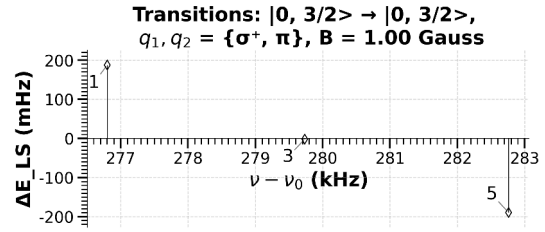
The following figures show the calculated spectra for different polarization configurations. Each set of four panels corresponds to a specific polarization pair, organized as follows: left column, $B = 0$ Gauss; right column, $B = 1$ Gauss; top row, transitions with $|3/2, M_J\rangle \rightarrow |3/2, M_J'\rangle$, bottom row, transitions with $|5/2, M_J\rangle \rightarrow |5/2, M_J'\rangle$. Please note that the labels within each panel are local and are not meant to be compared directly between panels.

These observations align with dipole selection rules and the expected behavior of tensor light shifts under linear and circular polarizations.

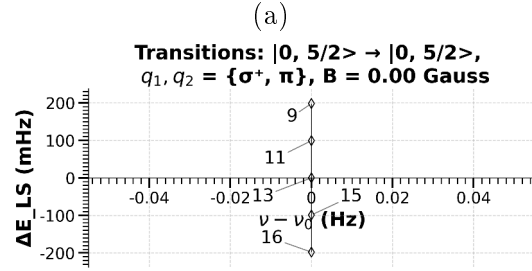
- The polarization pairs (π, σ^\pm) and (σ^\pm, π) yield the dominant off-diagonal light shifts relevant for Raman transitions. These produce shifts symmetric about $\Delta|M_J| = 0$, where transitions decreasing $|M_J|$ (e.g., $3/2 \rightarrow -1/2$) exhibit positive shifts, while those increasing $|M_J|$ (e.g., $1/2 \rightarrow 3/2$) show negative shifts.
- Other polarization configurations are not included, as they correspond either to scalar shifts (no differential energy change) or forbidden transitions under the selection rules relevant here.



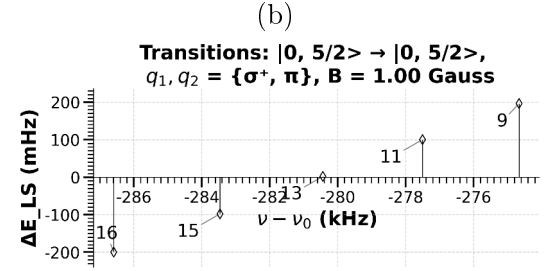
1. $|0, 3/2, -3/2\rangle \rightarrow |0, 3/2, -1/2\rangle$ 5. $|0, 3/2, 1/2\rangle \rightarrow |0, 3/2, 3/2\rangle$
3. $|0, 3/2, -1/2\rangle \rightarrow |0, 3/2, 1/2\rangle$



1. $|0, 3/2, -3/2\rangle \rightarrow |0, 3/2, -1/2\rangle$ 5. $|0, 3/2, 1/2\rangle \rightarrow |0, 3/2, 3/2\rangle$
3. $|0, 3/2, -1/2\rangle \rightarrow |0, 3/2, 1/2\rangle$



9. $|0, 5/2, -5/2\rangle \rightarrow |0, 5/2, -3/2\rangle$ 15. $|0, 5/2, 1/2\rangle \rightarrow |0, 5/2, 3/2\rangle$
11. $|0, 5/2, -3/2\rangle \rightarrow |0, 5/2, -1/2\rangle$ 16. $|0, 5/2, 3/2\rangle \rightarrow |0, 5/2, 5/2\rangle$
13. $|0, 5/2, -1/2\rangle \rightarrow |0, 5/2, 1/2\rangle$

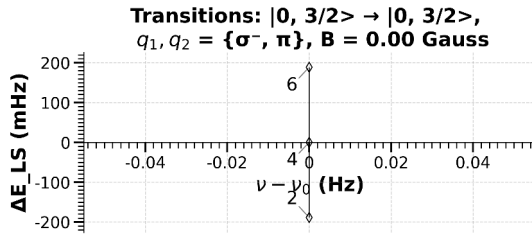


9. $|0, 5/2, -5/2\rangle \rightarrow |0, 5/2, -3/2\rangle$ 15. $|0, 5/2, 1/2\rangle \rightarrow |0, 5/2, 3/2\rangle$
11. $|0, 5/2, -3/2\rangle \rightarrow |0, 5/2, -1/2\rangle$ 16. $|0, 5/2, 3/2\rangle \rightarrow |0, 5/2, 5/2\rangle$
13. $|0, 5/2, -1/2\rangle \rightarrow |0, 5/2, 1/2\rangle$

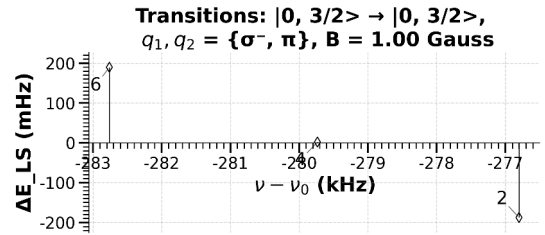
(c)

(d)

(e) Polarization configuration (σ^+, π)



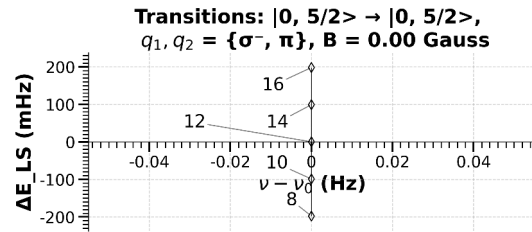
2. $|0, 3/2, -1/2\rangle \rightarrow |0, 3/2, -3/2\rangle$ 6. $|0, 3/2, 3/2\rangle \rightarrow |0, 3/2, 1/2\rangle$
4. $|0, 3/2, 1/2\rangle \rightarrow |0, 3/2, -1/2\rangle$



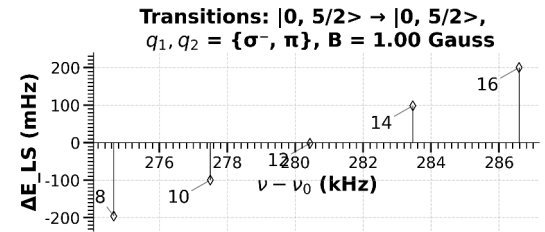
2. $|0, 3/2, -1/2\rangle \rightarrow |0, 3/2, -3/2\rangle$ 6. $|0, 3/2, 3/2\rangle \rightarrow |0, 3/2, 1/2\rangle$
4. $|0, 3/2, 1/2\rangle \rightarrow |0, 3/2, -1/2\rangle$

(f)

(g)



8. $|0, 5/2, -3/2\rangle \rightarrow |0, 5/2, -5/2\rangle$ 14. $|0, 5/2, 3/2\rangle \rightarrow |0, 5/2, 1/2\rangle$
10. $|0, 5/2, -1/2\rangle \rightarrow |0, 5/2, -3/2\rangle$ 16. $|0, 5/2, 5/2\rangle \rightarrow |0, 5/2, 3/2\rangle$
12. $|0, 5/2, 1/2\rangle \rightarrow |0, 5/2, -1/2\rangle$



8. $|0, 5/2, -3/2\rangle \rightarrow |0, 5/2, -5/2\rangle$ 14. $|0, 5/2, 3/2\rangle \rightarrow |0, 5/2, 1/2\rangle$
10. $|0, 5/2, -1/2\rangle \rightarrow |0, 5/2, -3/2\rangle$ 16. $|0, 5/2, 5/2\rangle \rightarrow |0, 5/2, 3/2\rangle$
12. $|0, 5/2, 1/2\rangle \rightarrow |0, 5/2, -1/2\rangle$

(h)

(i)

(j) Polarization configuration (σ^-, π)

Figure 3.8: Raman light shifts for two polarization configurations. Each subpanel shows the corresponding magnetic field strength and transition type. Local labels are not comparable across panels.

VI.2 Behavior for $\bar{J} = 3/2$

For the (σ^+, π) polarization, the transition $|3/2, -3/2\rangle \rightarrow |3/2, -1/2\rangle$ experiences a light shift of approximately 0.19 Hz, while $|3/2, -1/2\rangle \rightarrow |3/2, 1/2\rangle$ shows a negligible shift near zero, and $|3/2, 1/2\rangle \rightarrow |3/2, 3/2\rangle$ experiences a shift of about -0.19 Hz (Figure 3.8 (a) and (b)). The (σ^-, π) polarization yields a symmetric behavior: $|3/2, 3/2\rangle \rightarrow |3/2, 1/2\rangle$ has a light shift around 0.19 Hz, $|3/2, 1/2\rangle \rightarrow |3/2, -1/2\rangle$ is negligible, and $|3/2, -1/2\rangle \rightarrow |3/2, -3/2\rangle$ shows a shift near -0.18 Hz. This near mirror symmetry confirms the expected polarizability patterns, with null shifts at $M_J = \pm 1/2$ corresponding to vanishing differential light shifts between these sublevels (Figure 3.8 (f) and (g)).

VI.3 Behavior for $\bar{J} = 5/2$

For (σ^+, π) polarization, the light shifts follow a clear trend where the extremal transitions exhibit the largest magnitudes: $|5/2, 3/2\rangle \rightarrow |5/2, 5/2\rangle$ shows approximately -0.2 Hz, while $|5/2, 1/2\rangle \rightarrow |5/2, 3/2\rangle$ is around -0.1 Hz and slightly decreases with increasing magnetic field. The transition $|5/2, -1/2\rangle \rightarrow |5/2, 1/2\rangle$ remains negligible, whereas $|5/2, -3/2\rangle \rightarrow |5/2, -1/2\rangle$ exhibits a positive shift of about 0.1 Hz that grows slightly with the magnetic field, and $|5/2, -5/2\rangle \rightarrow |5/2, -3/2\rangle$ shows the largest positive shift around 0.2 Hz (Figure 3.8 (c) and (d)).

For (σ^-, π) polarization, the pattern is reversed with respect to the sign of M_J : $|5/2, -3/2\rangle \rightarrow |5/2, -5/2\rangle$ has a shift near -0.2 Hz, $|5/2, -1/2\rangle \rightarrow |5/2, -3/2\rangle$ is around -0.1 Hz and increases with field strength, $|5/2, 1/2\rangle \rightarrow |5/2, -1/2\rangle$ is negligible and decreases slightly with magnetic field, $|5/2, 3/2\rangle \rightarrow |5/2, 1/2\rangle$ is about 0.1 Hz and decreases with field, and $|5/2, 5/2\rangle \rightarrow |5/2, 3/2\rangle$ is about 0.2 Hz. This antisymmetry with respect to $M_J \rightarrow -M_J$ and the near-zero shifts around $M_J = \pm 1/2$ reflect the expected tensor light-shift structure and the minima in the differential polarizability gradient (Figure 3.8 (h) and (i)).

VI.4 Magnetic Field Dependence

Overall, the computed light shifts for the Raman transitions remain extremely small, typically in the sub-Hz range over the magnetic field interval of 0 to 1 Gauss. This behavior is primarily due to the strong cancellation between the ac Stark shifts of the initial and final states, which share the same electronic, vibrational, and rotational structure. For the two-photon transitions between different vibrational levels, a similar cancellation occurs because the electronic and rotational structures are identical in both states.

The residual variations observed (less than 0.05 Hz across the range) are therefore minor and mainly reflect the small difference in polarizability between the coupled states, rather than any substantial modification of the underlying tensor components with the magnetic field. Although these variations are negligible for most practical purposes, they become relevant when aiming for sub-Hz precision.

Chapter 4

Conclusion

We have presented a comprehensive analysis of two-photon rovibrational spectroscopy in H_2^+ , combining accurate calculations of dissociation energies, transition probabilities, Raman Rabi frequencies, and Zeeman shifts under various laser polarizations and magnetic sublevels. The computed dissociation energies,

$$E_{\text{dis}}(\nu = 0, L = 2) \approx -2.6290924577 \text{ eV}, \quad E_{\text{dis}}(\nu = 1, L = 2) \approx -2.3585684489 \text{ eV},$$

confirm that the states under study belong to the low-lying rovibrational levels of the $1s\sigma_g$ potential. The energy difference $\Delta E_{\text{dis}} \approx 0.270524 \text{ eV}$ corresponds to a two-photon transition frequency of approximately $\nu_{2\gamma} = \frac{\Delta E_{\text{dis}}}{2h} \simeq 32.7062 \text{ THz}$, which sets the requirements for laser frequency stabilization in high-precision spectroscopy.

A key finding is the very small magnetic-field sensitivity of transitions satisfying $q_1 + q_2 = 0$. For magnetic fields $B \lesssim 0.1 \text{ G}$, the Zeeman shift remains below $\Delta\nu_Z < 6 \text{ Hz}$, corresponding to a relative shift below 10^{-13} with respect to the two-photon excitation frequency ($2 \times 32.7 \text{ THz} = 65.4 \text{ THz}$). This remarkable insensitivity to magnetic perturbations is a crucial asset for precision measurements.

The calculated two-photon transition matrix elements at a test wavelength of $1.5 \mu\text{m}$,

$$\langle 0, 2|Q^{(0)}|1, 2\rangle = -0.547278, \quad \langle 0, 2|Q^{(2)}|1, 2\rangle = 0.422419,$$

are slightly larger than previously reported values [5], but they correctly reproduce the known static polarizabilities, indicating that the discrepancy arises from numerical convergence rather than physical modeling.

AC Stark shifts are found to be negligible for realistic laser intensities. For example, at $I = 0.1 \text{ W/mm}^2$, the induced frequency shifts are on the order of Hz or mHz, far below the kHz–MHz scale of the intrinsic linewidths. Their polarization dependence (negative for (π, π) , positive for (σ^\pm, σ^\mp) , and asymmetric for mixed configurations) reflects the interplay of scalar and tensor polarizabilities but has no significant impact on the achievable accuracy.

In conclusion, (π, π) -polarized lasers driving two-photon rovibrational transitions of H_2^+ (with photon wavelength $\lambda \approx 9.17 \mu\text{m}$) offer particularly favorable conditions for high-precision spectroscopy. These transitions combine strong excitation probabilities, extremely low Zeeman sensitivity (sub-10 Hz at 0.1 G), and minimal light shifts, making them ideally suited for frequency metrology and fundamental tests with molecular ions. For Raman transitions between hyperfine or Zeeman sublevels within the same rovibrational level ($\nu = 0, L = 2$), similar advantages are found, with the added flexibility of choosing the photon wavelength (e.g., near $1.5 \mu\text{m}$) to optimize laser performance and minimize systematic effects.

Bibliography

- [1] CODATA Value: Electron-proton mass ratio. https://physics.nist.gov/cgi-bin/cuu/Value?mesmp|search_for=electron+mass.
- [2] Osama Terra. Femtosecond Lasers for Optical Frequency Measurement. *Journal of Measurement Science and Applications (JMSA)*, 2(2):2–15, August 2022.
- [3] Maxime Leuliet. Spectroscopie moléculaire à quelques Hz près : Test sur HCOOH et spectroscopie de H_2^+ pour la détermination des constantes fondamentales, March 2025.
- [4] Johannes Heinrich. *A Be^+ Ion Trap for H_2^+ Spectroscopy*. PhD thesis, Sorbonne Université, April 2018.
- [5] J. Ph. Karr. H_2^+ and HD^+ : Candidates for a molecular clock. *Journal of Molecular Spectroscopy*, 300:37–43, June 2014.
- [6] Jean-Philippe Karr, Franck Bielsa, Albane Douillet, Jofre Pedregosa Gutierrez, Vladimir I. Korobov, and Laurent Hilico. Vibrational spectroscopy of H_2^+ : Hyperfine structure of two-photon transitions. *Physical Review A*, 77(6):063410, June 2008.
- [7] Jean-Philippe Karr, Vladimir I. Korobov, and Laurent Hilico. Vibrational spectroscopy of H_2^+ : Precise evaluation of the Zeeman effect. *Physical Review A*, 77(6):062507, June 2008.
- [8] Fundamental Physical Constants from NIST. <https://physics.nist.gov/cuu/Constants/index.html>.
- [9] Cédric Delaunay, Jean-Philippe Karr, Teppei Kitahara, Jeroen C. J. Koelemeij, Yotam Soreq, and Jure Zupan. Self-Consistent Extraction of Spectroscopic Bounds on Light New Physics. *Physical Review Letters*, 130(12):121801, March 2023.
- [10] J.-Ph. Karr, L. Hilico, and Vladimir I. Korobov. One-loop vacuum polarization at $m\alpha^7$ and higher orders for three-body molecular systems. *Physical Review A*, 95(4):042514, April 2017.
- [11] Sayan Patra, M. Germann, J.-Ph. Karr, M. Haidar, L. Hilico, V. I. Korobov, F. M. J. Cozijn, K. S. E. Eikema, W. Ubachs, and J. C. J. Koelemeij. Proton-electron mass ratio from laser spectroscopy of HD^+ at the part-per-trillion level. *Science*, 369(6508):1238–1241, September 2020.

- [12] S. Alighanbari, I. V. Kortunov, G. S. Giri, and S. Schiller. Test of charged baryon interaction with high-resolution vibrational spectroscopy of molecular hydrogen ions. *Nature Physics*, 19(9):1263–1269, September 2023.
- [13] Vladimir I. Korobov, L. Hilico, and J.-Ph. Karr. Fundamental Transitions and Ionization Energies of the Hydrogen Molecular Ions with Few ppt Uncertainty. *Physical Review Letters*, 118(23):233001, June 2017.
- [14] Refimeve.
- [15] Abdessamad Mbardi. *Spectroscopie d'ions H_2^+ Piégés : Développement d'un Laser à 9.17 μm Référencé Au Système International d'unité*. These de doctorat, Sorbonne université, December 2023.
- [16] L. M. Wang and Z.-C. Yan. Relativistic corrections to the ground state of H_2 calculated without using the Born-Oppenheimer approximation. *Physical Review A*, 97(6):060501, June 2018.
- [17] Dimitar Bakalov, Vladimir Korobov, and Stephan Schiller. Precision spectroscopy of the molecular ion HD^+ : Control of Zeeman shifts. *Physical Review A*, 82(5):055401, November 2010.
- [18] CODATA Value: Hartree energy in eV. https://physics.nist.gov/cgi-bin/cuu/Value?hrev|search_for=hartree.
- [19] Sahil Viel. Probing Fundamental Physics with H_2^+ . Internship Report, Sorbonne Université, Laboratoire Kastler Brossel, Équipe Ions Piégés, Paris, France, July 2024.
- [20] Gilbert Grynberg. *Spectroscopie d'absorption à deux photons sans élargissement Doppler. Application à l'étude du sodium et du néon*. PhD thesis, Université Pierre et Marie Curie - Paris VI, January 1976.
- [21] Albert Messiah. *Quantum Mechanics: Two Volumes Bound as One*. Dover Publications, 1999.
- [22] V. I. Korobov, D. Bakalov, and H. J. Monkhorst. Variational expansion for antiprotonic helium atoms. *Physical Review A*, 59(2):R919–R921, February 1999.
- [23] Nicolas Sillitoe. *Production of State-Selected H_2^+ Ions and Numerical Simulations of Sympathetic Cooling in RF Traps*. PhD thesis, Université Pierre et Marie Curie, November 2017.

Appendix A

Wave Functions Variational Calculation

We employ a variational approach based on the method proposed by [22], which constructs a trial wavefunction with variational parameters and minimizes the expectation value of the Hamiltonian to approximate the bound or resonant state energies of the system.

The total wavefunction, introduced in Eq. (2.3), $\Psi_{LM}^{\Pi}(\mathbf{R}, \mathbf{r}_1)$, is expanded in a basis of coupled spherical harmonics and radial functions. The angular dependence is described by bipolar harmonics, while the radial part incorporates correlation functions that capture the dynamical behavior of the three-body system.

The exponents α_n , β_n , and γ_n in the radial function expansion are complex numbers chosen in a quasi-random manner to ensure both completeness and rapid convergence. The use of complex exponentials is particularly advantageous for describing oscillatory structures and the nodal patterns characteristic of resonant or molecular-like states.

A general trial wavefunction is constructed as a linear combination of atomic- and molecular-like components. It is expressed as:

$$\Psi_{MLL}(\mathbf{R}, \mathbf{r}) = \sum_{l_1+l_2=L} R^{l_1} r^{l_2} [Y_{l_1} \otimes Y_{l_2}]_{LM} G_{l_1 l_2 L}(R, r, u),$$

where the radial function takes the form:

$$G_{l_1 l_2 L}(R, r, u) = \sum_i \left[C_i \cos(n_i R) + D_i \sin(n_i R) \right] e^{-a_i R - b_i r - g_i u},$$

with the parameters a_i , b_i , g_i , and n_i also chosen quasi-randomly. The inclusion of oscillatory functions $\cos(n_i R)$ and $\sin(n_i R)$ enhances the flexibility of the basis in representing the nodal structure of molecular orbitals and vibrational states.

The variational problem reduces to solving the generalized eigenvalue equation:

$$A\mathbf{c} = E B\mathbf{c},$$

where A and B are real symmetric matrices of size $2N \times 2N$ (with N being the number of basis functions), and \mathbf{c} is the vector of expansion coefficients. For each chosen set of complex variational parameters, the program constructs and diagonalizes the matrix pair (A, B) , extracting the eigenvalues and normalizing the corresponding eigenvectors.

Appendix B

Linear Paul Trap

A Paul trap confines charged particles using a time-dependent quadrupole potential. By applying oscillating radio-frequency (RF) electric fields, it creates an effective, time-averaged potential that leads to stable confinement. The general electrostatic potential has the quadrupolar form:

$$\Phi(x, y, z) = \alpha x^2 + \beta y^2 + \gamma z^2, \quad (\text{B.1})$$

and Laplace's equation in free space imposes the condition:

$$\alpha + \beta + \gamma = 0. \quad (\text{B.2})$$

This constraint, in line with Earnshaw's theorem, implies that a static electrostatic potential cannot trap a charged particle in all three spatial dimensions simultaneously—at least one direction must be deconfining. The Paul trap overcomes this limitation by dynamically switching the confinement axes using an RF field. When averaged over one oscillation period, this produces a net confining effect.

In other words, it is impossible for all second derivatives (curvatures) of the potential to be simultaneously positive. The alternating RF fields continuously rotate the confinement directions, such that the particle experiences overall stability over time.

I Linear Paul Trap

In practice, a common implementation of this principle is the linear Paul trap, which employs a 2D quadrupole potential:

$$\Phi(x, y, t) = \frac{V(t)}{2r_0^2}(x^2 - y^2), \quad (\text{B.3})$$

where $V(t) = U - V \cos(\Omega t)$ includes both a static (DC) component U and an RF component $V \cos(\Omega t)$. This potential does not vary along the z -axis, which remains unconfined.

The force is obtained via $\mathbf{F} = -q\nabla\Phi$, leading to the equations of motion [4]:

$$m\ddot{x} = \frac{q}{r_0^2}[U - V \cos(\Omega t)]x, \quad m\ddot{y} = -\frac{q}{r_0^2}[U - V \cos(\Omega t)]y, \quad \ddot{z} = 0.$$

Introducing the dimensionless parameters:

$$\tau = \frac{\Omega t}{2}, \quad a = \frac{4qU}{mr_0^2\Omega^2}, \quad q = \frac{2qV}{mr_0^2\Omega^2},$$

we obtain the Mathieu equations:

$$\frac{d^2x}{d\tau^2} + [a - 2q \cos(2\tau)]x = 0, \quad \frac{d^2y}{d\tau^2} + [-a + 2q \cos(2\tau)]y = 0.$$

The solutions are stable only within specific regions of the (a, q) stability diagram.

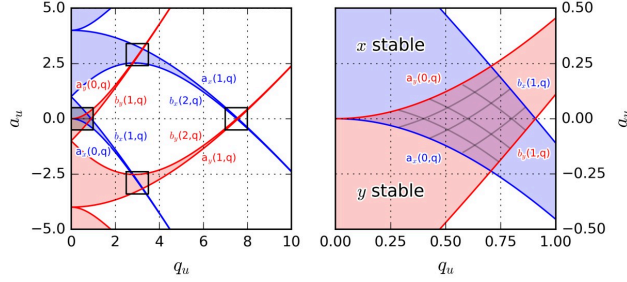


Figure B.1: Stability diagram of the Mathieu equation for a linear RF trap [4]. Left: overlapping regions define stable solutions. Right: the first stable region.

I.1 Adiabatic Approximation and Micromotion

When $a \ll 1$ and $q^2 \ll 1$, the ion motion can be separated into $\mathbf{r}(t) = \mathbf{R}(t) + \xi(t)$, where $\mathbf{R}(t)$ describes the slow secular motion, and $\xi(t)$ is the fast micromotion at frequency Ω [23]. The total electric field is $\mathbf{E}(t) = \mathbf{E}_0 + \mathbf{E}_\Omega(t)$, where \mathbf{E}_0 is a static component, and $\mathbf{E}_\Omega(t)$ is the RF field driving the micromotion. Averaging over one RF cycle leads to the ponderomotive potential:

$$\Phi_{\text{eff}}(\mathbf{r}) = \frac{q^2}{4m\Omega^2} |\mathbf{E}_\Omega(\mathbf{r})|^2, \quad (\text{B.4})$$

with an associated averaged force $\langle \mathbf{F}_{\text{RF}} \rangle = -\frac{q^2}{4m\Omega^2} \nabla |\mathbf{E}_\Omega|^2$. The resulting secular motion is harmonic, with effective frequencies:

$$\omega_{x,y}^2 = \frac{\Omega^2}{4} \left(a \pm \frac{q^2}{2} \right). \quad (\text{B.5})$$

I.2 Endcap Potential and Axial Confinement

To confine ions along z , additional static potentials are applied to *endcap electrodes*:

$$\Phi_{\text{endcap}}(x, y, z) = \frac{U_1}{2z_{\text{eff}}^2} \left(z^2 - \frac{x^2 + y^2}{2} \right), \quad (\text{B.6})$$

resulting in axial harmonic motion:

$$\ddot{z} + \omega_z^2 z = 0, \quad \omega_z^2 = \frac{2qU_1}{mz_{\text{eff}}^2}. \quad (\text{B.7})$$

Appendix C

Supplementary Results: Complete Data Sets for Two-Photon and Raman Calculations

For completeness, this appendix compiles the full set of numerical results generated from the calculations of the Two Photon operator described in Chapters 2 and 3. Although these complete results are not analyzed in detail in the main text, they follow the same selection rule patterns and general trends discussed in Chapter 3. They are provided here as a reference and for potential future analysis of specific transitions of experimental interest.

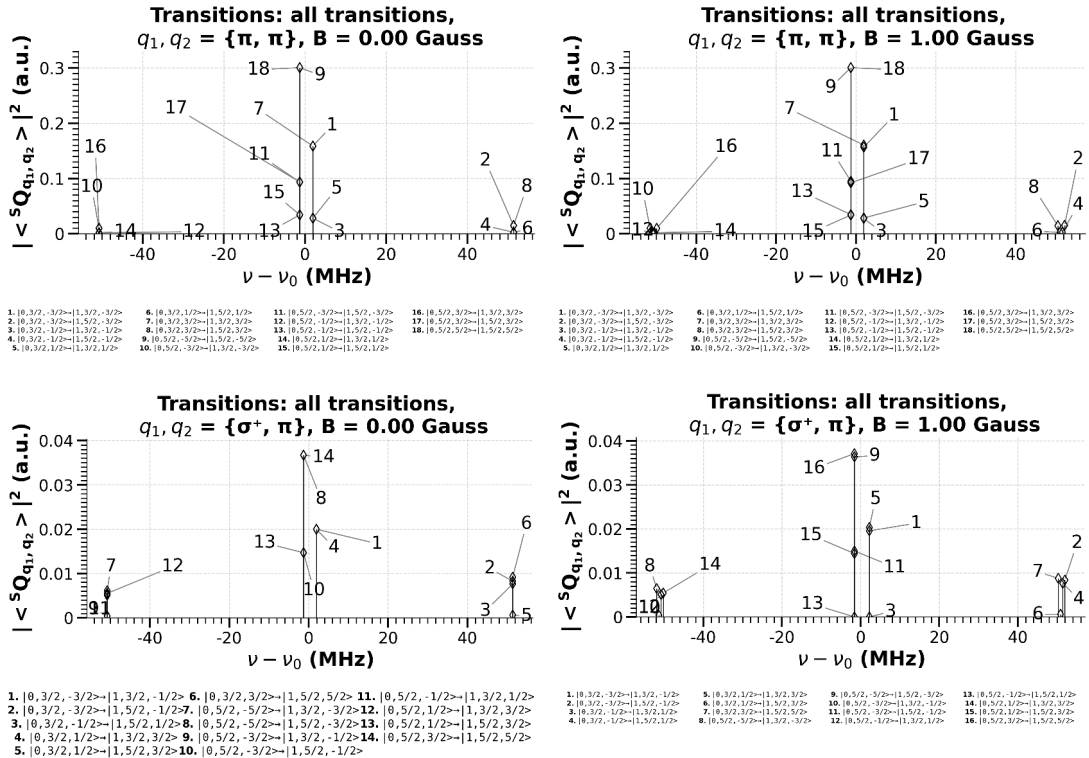


Figure C.1: Comprehensive results for two-photon transition probabilities for all polarization configurations (q_1, q_2) and magnetic fields $B = 0$ and 1G. Local labels within each panel are not directly comparable across different subfigures.

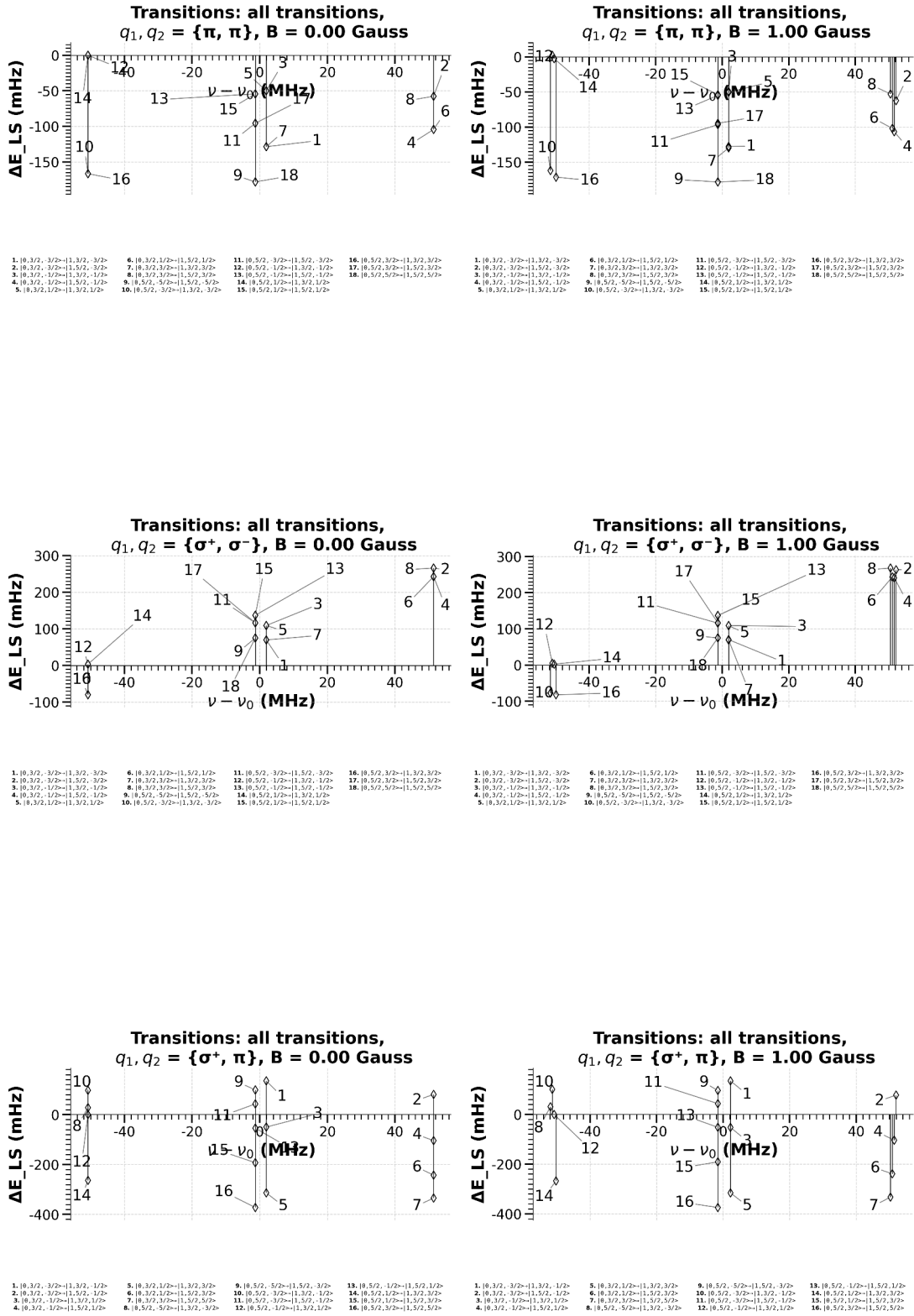


Figure C.3: Comprehensive results for two-photon light shifts for all polarization configurations (q_1, q_2) and magnetic fields $B = 0$ and 1 G. Local labels within each panel are not directly comparable across different subfigures.

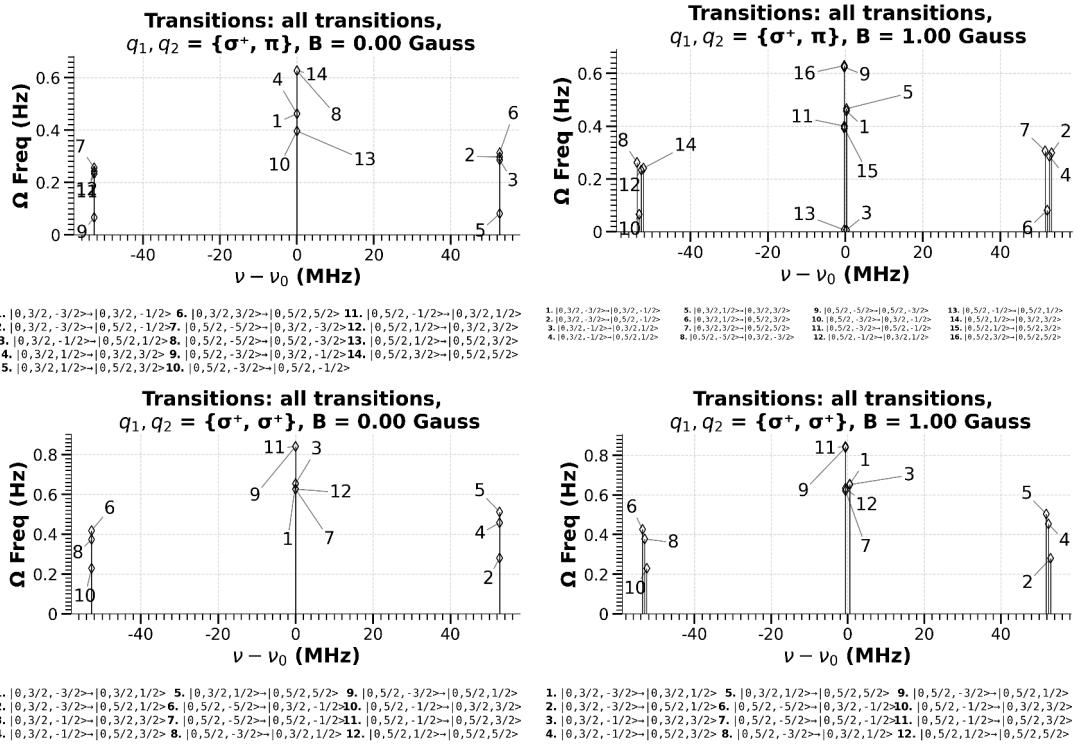


Figure C.4: Comprehensive results for Raman Rabi Frequencies for all polarization configurations (q_1, q_2) and magnetic fields $B = 0$ and 1 G. Local labels within each panel are not directly comparable across different subfigures.

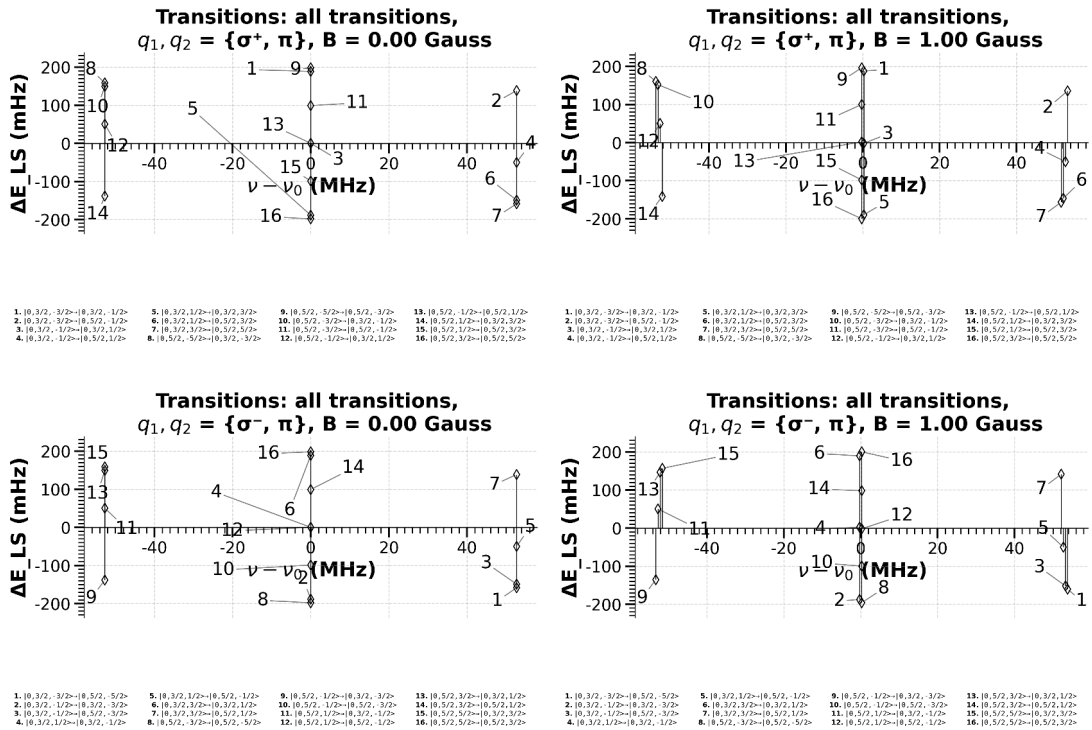


Figure C.5: Comprehensive results for Raman light shifts for all polarization configurations (q_1, q_2) and magnetic fields $B = 0$ and 1 G. Local labels within each panel are not directly comparable across different subfigures.